International Journal of Mechanical Sciences 275 (2024) 109309

Contents lists available at ScienceDirect

International Journal of Mechanical Sciences

journal homepage: www.elsevier.com/locate/ijmecsci

4D-printed reusable metamaterial via shape memory effect for energy dissipation

Di Zhang [a], Meiyu Li [a], Na Qiu [b], Jie Yang [b], Chi Wu [c], Grant Steven [c], Qing Li [c], Jianguang Fang [a,*]

[a] *School of Civil and Environmental Engineering, University of Technology Sydney, Sydney, NSW 2007, Australia*
[b] *Mechanical and Electrical Engineering College, Hainan University, Haikou 570228, China*
[c] *School of Aerospace, Mechanical and Mechatronic Engineering, The University of Sydney, Sydney, NSW 2006, Australia*

ARTICLE INFO

Keywords:
4D printing
Honeycomb metamaterials
Energy dissipation
Shape memory effect
Reusability
Mechanical degradation

ABSTRACT

The present study aims at developing reusable metamaterials fabricated by 4D printing technology. Honeycomb metamaterials were manufactured via fused deposition modeling (FDM) with shape memory polymers (SMPs). The reusability of these metamaterials was determined through cyclic cold programming experiments, where each cycle involved a loading-unloading-heating (shape recovery)-cooling process. The novelty of this paper lies not only in experimentally demonstrating the recoverability of metamaterials by reversing plastic deformation based on the shape memory effect of SMPs, but also in studying their reusability of SMP metamaterials under cyclic programming and the effect of printing materials and unit-cell types on the mechanical degradation. The results reveal that, under one single compression cycle, the polylactic acid (PLA) hexagonal honeycomb dissipated 22% more energy than the polyethylene terephthalate glycol (PETG) counterpart because the higher elastic modulus of PLA leads to a larger critical buckling load for segments in honeycomb structures. Furthermore, the PETG re-entrant honeycomb dissipated 25% more energy than the hexagonal counterpart due to its negative Poisson's ratio and the overall uniform deformation pattern. More importantly, it is found that under multiple compression cycles, the PETG hexagonal honeycomb maintained an energy dissipation capacity of 78.3% at Cycle 6, nearly 3.5 times that of the PLA counterpart as a result of the better ductility of PETG. Moreover, the PETG re-entrant honeycomb could be reused for 17 cycles, while the hexagonal counterpart could only be reused for 12 cycles. This is because the re-entrant unit cells are failure-resistant and of less concentration in plastic deformation. The results demonstrate that the constituent materials with better ductility and the unit-cells with more failure resistance can reduce mechanical degradation, thereby exhibiting better reusability of metamaterials.

1. Introduction

Mechanical metamaterials exhibit exceptional physical behaviors, usually unavailable in nature and counterintuitive in practice [1–5]. Fueled by fast-expanding design and fabrication capacity, researchers have been able to conceive some novel metamaterials over the last few decades, such as different auxeticities [6–9], negative mechanical properties [10–13], and extremal multifunctional characteristics (e.g., stiffness, strength, low mass density, etc.) [14–16].

Normally, traditional manufacturing technologies are not applicable in fabricating mechanical metamaterials due to their sophisticated topological structures [4,17,18]. However, the emergence of additive manufacturing, or 3D printing, has made it possible to manufacture metamaterials with complex topologies, greatly facilitating the studies in mechanical metamaterials. 3D printing is a computer-aided manufacturing process that enables the building of three-dimensional structures by feeding, bonding, and solidifying constituent materials in a layer-by-layer fashion [19]. With the help of 3D printing, mechanical metamaterials have been applied in automotive [9,14,20–22], aerospace [23–25], and biomedical engineering [3,26–28].

One symbolic application for mechanical metamaterials is energy dissipation because their light weight can potentially offer unrivaled specific energy absorption (SEA) [4]. The energy dissipation in traditional mechanical metamaterials is typically achieved through severe

* Corresponding author.
E-mail address: Jianguang.Fang@uts.edu.au (J. Fang).

https://doi.org/10.1016/j.ijmecsci.2024.109309
Received 19 September 2023; Received in revised form 30 March 2024; Accepted 19 April 2024
Available online 20 April 2024

plastic deformation and material damage, both of which are permanent and irreversible to those materials [29,30]. Therefore, traditional mechanical metamaterials used for energy dissipation often exhibit characteristics of one-off service life. In order to achieve the purpose of recurring energy dissipation in mechanical metamaterials, alternative energy dissipation mechanisms have been explored [31], such as friction [30,32,33], instability-induced energy trapping and dissipation [34–38], or combination of them [39,40]. However, while achieving reusability, instability-based metamaterials commonly exhibit poor load-bearing capacity because they require structures with a small thickness ratio [30], and friction-based metamaterials may suffer from surface wear [32]. More importantly, such metamaterials may offer limited energy dissipation, as in most cases, their constituent materials are not allowed to go beyond the elastic region [30,32,36].

To achieve the goal of reusability and significant energy dissipation, one of the most straightforward approaches may be to find constituent materials that are capable of reversing plastic deformation. The emergence of 4D printing has made this approach possible [41–45]. Unlike the traditional materials used in 3D printing, the materials adopted by 4D printing are normally stimulus-responsive, allowing fabricated samples to change their shape even after the printing process. Shape memory polymers (SMPs) signify one of the most popular and widely used constituent materials in 4D printing. SMPs are heat-responsive and capable of recovering their plastic deformation through the shape memory effect (SME) after a simple heating process [46–48].

In recent years, some SMP metamaterials capable of dissipating energy by reversing plastic deformation through the shape memory effect have been reported. For example, Namvar et al. [29] fabricated SMP honeycomb metamaterials with different Poisson's ratios, all of which exhibited a 100% shape recovery after a simple heating process. Xu et al. [49] also investigated these honeycomb metamaterials and found the geometric configuration had an impact on their shape recoverability. Wan et al. [50] fabricated cylindrical SMP metamaterials with horseshoe-shaped unit cells and demonstrated their capability to recover to their original shape after stretching or bending. Zeng et al. [51] also studied horseshoe-shaped metamaterials and reported that using continuous fiber-reinforced composites (CFRCs) as the printing material not only provided remarkable shape recovery but also enhanced the energy dissipating capability for metamaterials. Dong et al. [52] reported a shape recovery ratio above 90% over the first six cycles on the metamaterials printed by CFRCs. Wan et al. [53] fabricated SMP origami metamaterials capable of recovering from the temporary folded shapes to the original shapes after reheating. Hamzehei et al. [54] revealed the good recoverability of the zero Poisson's ratio (ZPR) metamaterials and recognized the mechanical degradation of metamaterials from the force-displacement curves through two consecutive compression cycles.

However, the above-mentioned studies mainly focused on the shape recoverability of metamaterials and have not extensively explored their reusability subject to multiple loading cycles. The reusability of metamaterials indicates their capability to maintain the energy dissipation level after being mechanically deformed and thermally recovered. In other words, SMP-based metamaterials can be only regarded as reusable when they exhibit minor mechanical degradation after loading-unloading-heating cycles. To date, there have been few studies on the reusability of SMP metamaterials [55–57]. Moreover, the impact of the constituent material and the unit-cell geometry on the reusability of these metamaterials remains unclear.

This study aims to develop reusable energy-dissipating metamaterials with different constituent materials and unit-cell configurations by carrying out cyclic compression-recovery tests on the metamaterials. Factors affecting the mechanical degradation of metamaterials during cyclic usage are revealed by comprehensively recording and analyzing the performance of metamaterials in each cycle. It is anticipated to gain new insight and develop a framework for the design of reusable lightweight metamaterials for energy dissipation. The remainder of this paper is organized as follows. Section 2 introduces the design and fabrication of honeycomb metamaterials, as well as the experimental protocols for the cyclic cold programming tests. Section 3 presents the mechanical analysis of the metamaterials under one-off compression tests and elaborates the reusability of metamaterials under cyclic loading process. Section 4 summarizes the research findings and provides an outlook for future research.

2. Materials and methods

In this section, the design method for honeycomb metamaterials with different Poisson's ratios is introduced first. Then, the 4D printing process of FDM fabricated honeycomb samples using SMPs as printing materials is explained. Last, the detailed steps involved in the cyclic cold programming process are presented.

2.1. Design of honeycomb structures

The metamaterials to be investigated in this study are honeycomb structures for their characteristic features and practical popularity. They can be easily fabricated by FDM printers or other techniques. Honeycombs with three different unit-cell structures were considered, including the hexagonal honeycomb with positive Poisson's ratio, the hybrid honeycomb with zero Poisson's ratio, and the re-entrant honeycomb with negative Poisson's ratio. Fig. 1**(a)** illustrates the geometric configurations of these three honeycombs. Note that a width (building height) of 12 mm was used here to avoid out-of-plane instability during in-plane compressions.

2.2. 4D fabrication materials and method

Shape memory polymers (SMPs) were used as the printing materials in this study as they can recover plastic deformation through the shape memory effect (SME), which enables the fabricated honeycombs to dissipate energy repetitively. The mechanism of the shape memory effect on the molecular level is illustrated in Fig. 2, where SMPs are regarded as networks composed of long molecular chains and netpoints. These netpoints are crosslinked either covalently or physically and function as switches [58]. Below a critical temperature known as the glassy transition temperature (T_g), the crosslinked netpoints are inactive and thus immobilize the movement of molecular chains, resulting in a glassy phase [46]. When SMPs are heated above T_g, the netpoints switch open, and the polymeric chains become flexible, leading to a rubbery phase [47]. Therefore, the plastic deformation introduced in the glassy phase of SMPs is recoverable once they are heated above T_g because polymeric chains are mobilized in the rubbery phase.

PLA (JGMAKER, China) and PETG (Polymaker, China) filaments were used to fabricate the honeycombs to investigate the effect of printing materials on the reusability of fabricated metamaterials. According to the material datasheet provided by the manufacturers, PLA has a T_g of approximately 65 °C, while PETG has a T_g of around 85 °C.

Ultimaker S3 FDM printer (Ultimaker, The Netherlands) was used to fabricate the designed honeycomb metamaterials. First, the CAD models were created in SolidWorks and then exported as STL files. These STL files were sliced using Cura (Ultimaker, Netherlands) to generate G-code files for 3D printing. The key printing parameters were set as follows: a layer height of 0.4 mm, a line width of 0.4 mm, an infill line distance of 0.4 mm, a concentric infill pattern, a printing speed of 50 mm/s, a nozzle temperature of 200 °C for PLA and 240 °C for PETG, respectively, and a building plate temperature of 60 °C for PLA and 80 °C for PETG, respectively. Finally, the G-code files were uploaded to the FDM printer for printing. Fig. 1**(b)** shows that a concentric infill pattern and an infill line distance of 0.4 mm result in a negative airgap value of −0.05 mm, which allows better mechanical performance of the fabricated honeycombs [59].

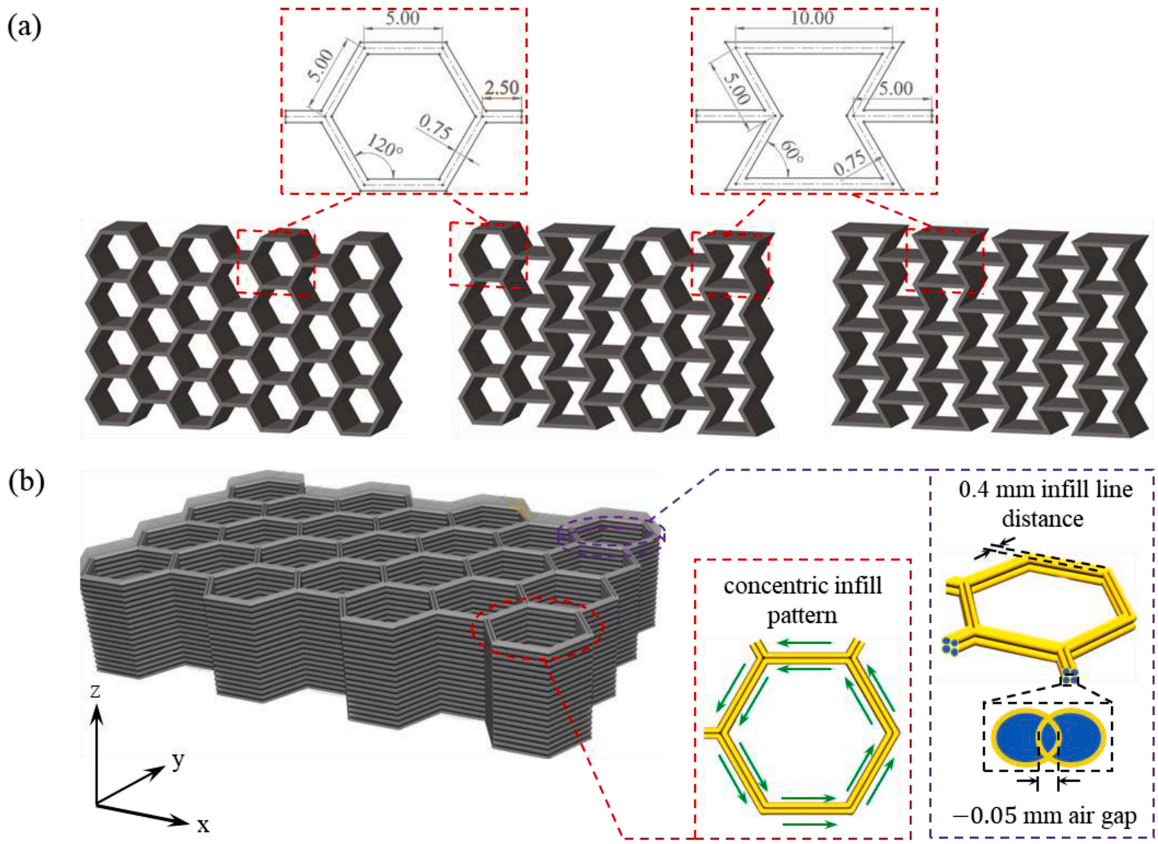

Fig. 1. (a) Structural profiles and dimensions of honeycomb metamaterials: the hexagonal honeycomb with positive Poisson's ratio (left), the hybrid honeycomb with zero Poisson's ratio (middle), and the re-entrant honeycomb with negative Poisson's ratio (right). (b) Infill pattern and air gap value for the FDM printing process.

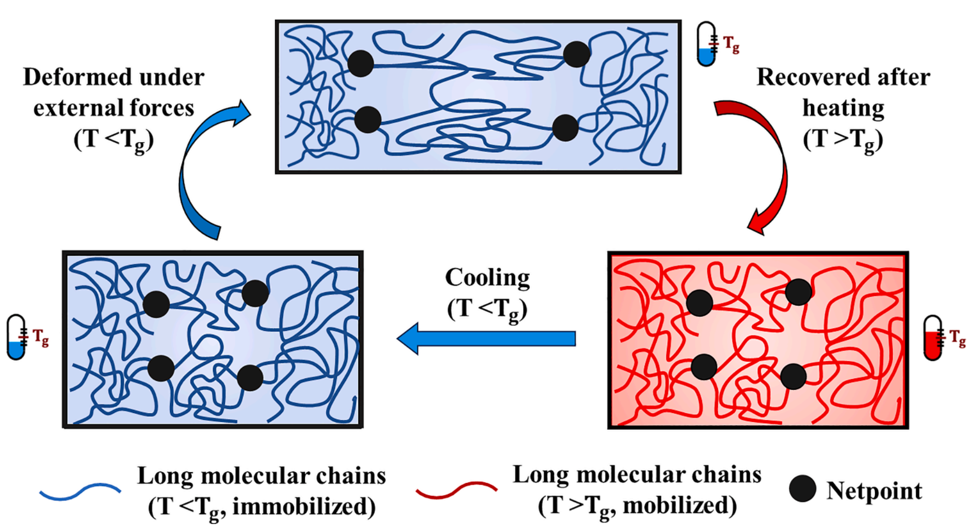

Fig. 2. Molecular mechanism of the thermally induced shape memory effect (SME) of shape memory polymers, T_g = glass transition temperature related to phase changes.

2.3. Experiment procedure and equipment setup

The reusability of metamaterials was characterized through a series of cold programming cycles. Fig. 3**(a)** illustrates the process of a single cold programming cycle, comprising four major steps [46]:

- Step 1: Loading process – The metamaterial samples were compressed at room temperature, below T_g of the SMPs.
- Step 2: Unloading process – The applied force was removed, allowing the metamaterial samples to reverse elastic deformation.
- Step 3: Shape recovery process – The metamaterial samples were heated above T_g to trigger the shape memory effect of the SMPs, leading them to recover their pre-programmed shape.
- Step 4: Cooling process - The heated samples were cooled down to their initial state (room temperature).

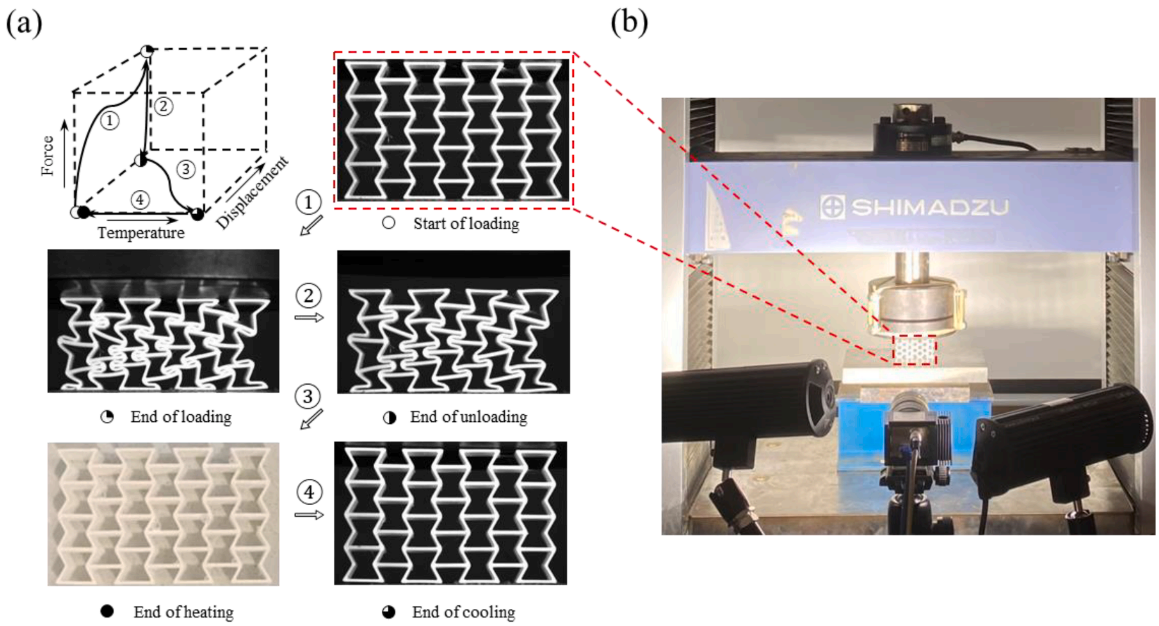

Fig. 3. (a) Schematic of a single cold-programming cycle. (b) Experimental setup for the compression tests. The cold programming of metamaterials is a loading-unloading-recovery-cooling process.

Fig. 3**(b)** illustrates the experimental setup for the compression tests. The loading in Step 1 and unloading in Step 2 were performed on an Autograph AGX universal testing machine (Shimadzu, Japan) at a speed of 3 mm/min to ensure quasi-static conditions and eliminate viscosity dependency by applying a low strain rate [60]. The deformation of metamaterial samples during the loading-unloading process was recorded using a MONET-3D camera (Sobriety, Czech Republic) at a rate of 0.5 frames per second, ensuring that shape changes resulting from every 0.1 mm displacement were captured. In Step 3, the heating of the metamaterial samples was achieved by placing the samples into a heating medium (water or air) with a temperature of 95 °C (above T_g). The heating process concluded when no further shape recovery was observed from the samples. This study selected water-bath heating as the heating method for the cyclic cold programming tests as the cyclic results revealed that water was not only more effective but also allowed for better shape recovery of honeycombs than air when working as the heating medium, as detailed in Section 3.2.2.

3. Results and discussion

In this section, the effect of printing materials and unit-cell structures on the mechanical performance and reusability of honeycomb metamaterials are investigated. Two polymers (i.e., PLA and PETG) and three unit-cell structures (i.e., hexagonal, hybrid, and re-entrant honeycombs) were considered. Section 3.1 presents the results of all honeycombs under the first cycle of compression to analyze the effect of these two factors (constituent materials and unit-cell structures) on the mechanical performance of metamaterials for one-off use. Section 3.2 analyzes the data derived from cyclic cold programming tests to investigate the effect of them on the reusability of metamaterials under multiple cycles.

3.1. One-off mechanical performance of metamaterials

This section discusses the effects of printing materials and unit-cell structures on the one-off mechanical characteristics of honeycomb metamaterials. All the experimental data was derived from one compression cycle with a loading distance of 12 mm (approximately 34% loading strain). The metrics used for analyzing the mechanical behavior are introduced first, followed by scrutinizing the effect of printing materials and unit-cell structures.

3.1.1. Metrics for mechanical performance analysis

The force-displacement responses obtained from the one-off cold programming tests were used to analyze the mechanical characteristics of honeycombs. Fig. 4**(a)** illustrates a typical force-displacement curve after one loading-unloading cycle. The loading curve starts from an elastic region, but reduces after the force reaches a peak, and then experiences a long plastic plateau. The load starts to be removed once the maximum displacement is reached, which also marks the beginning of the unloading curve. The unloading curve ends with a displacement significantly greater than zero, indicating that the metamaterial has undergone significant plastic deformation and, therefore, cannot recover most of the compressed height.

Four metrics are used to quantify the mechanical performance of honeycombs, including structural elastic stiffness (K_{stru}), initial peak force (F_{peak}), plateau force (F_{pl}), and total energy dissipation (E_{diss}). K_{stru} is determined from the elastic region of the force-displacement curve. F_{peak} is the first peak reached by the force. F_{pl} is the average force in the plateau region, which is defined as the region between the displacement at F_{peak} and the maximum loading displacement. E_{diss} is defined as the area between the loading and unloading curves of the force-displacement response, as shadowed in Fig. 4**(a)**.

3.1.2. Effect of printing materials

The tensile properties of PLA and PETG were determined from uniaxial tensile tests of material specimens in line with ASTM standard D638. All the uniaxial tension specimens were designed and fabricated by using type IV geometry with a thickness of 4 mm. The same printing parameters and FDM printer used for honeycomb samples (as detailed in Section 2.2) were adopted to fabricate uniaxial tension specimens, except that a line infill pattern with a raster angle of 0° (along the length direction) was used. Fig. 4**(b)** compares the tensile behavior between PLA and PETG, where PLA exhibits a greater elastic modulus (1.47 GPa) than PETG (0.70 GPa) and a higher tensile strength (43.5 MPa) than PETG (34.5 MPa). However, PETG shows better ductility with an elongation at a break of 7.6%, whereas PLA breaks at 4.8% elongation.

The effect of printing materials on the mechanical behavior of metamaterials was characterized by the testing results of honeycomb

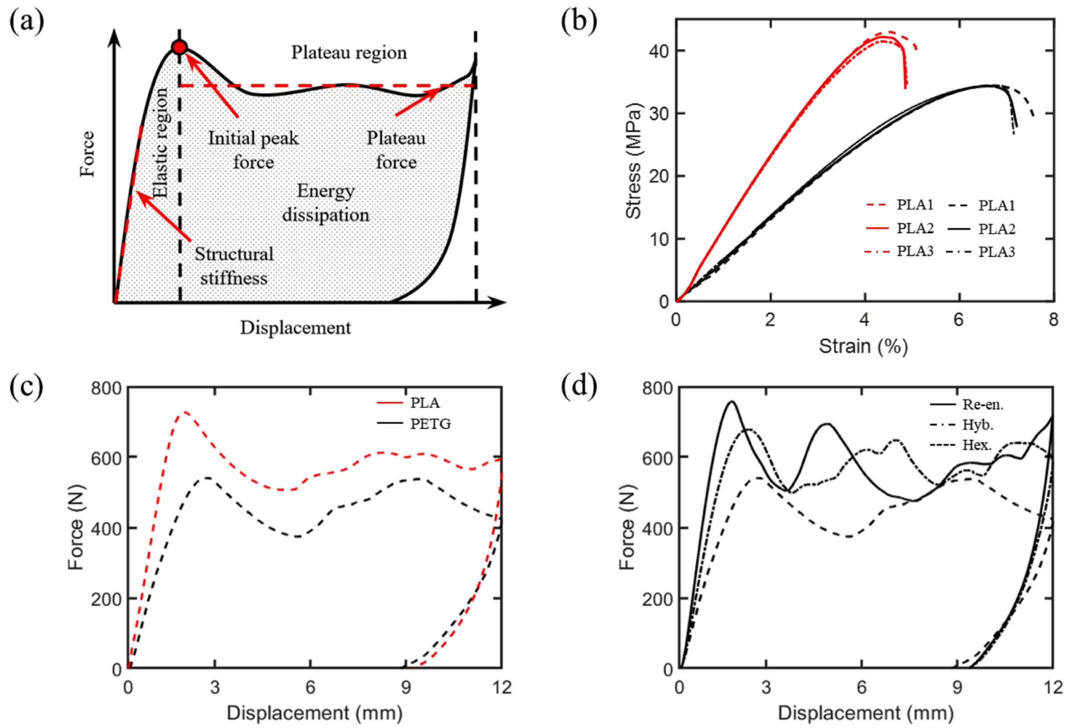

Fig. 4. (a) Typical force-displacement curve and the metrics for one-off mechanical performance analysis. (b) Strain-stress responses of the PLA and PETG tensile samples. PLA has higher elastic modulus and strength, while PETG offers better ductility. (c) The force-displacement responses of the PLA hexagonal honeycomb and the PETG hexagonal honeycomb from Cycle 1. The PLA hexagonal honeycomb has better mechanical performance than the PETG hexagonal honeycomb. (d) The force-displacement responses of the PETG hexagonal honeycomb, the PETG hybrid honeycomb, and the PETG re-entrant honeycomb from Cycle 1. The PETG re-entrant honeycomb has the best mechanical performance, followed by the PETG hybrid honeycomb, and then the PETG hexagonal honeycomb.

samples with the same unit-cell structure but printed using different materials, i.e., the PLA hexagonal honeycomb and the PETG hexagonal honeycomb. Fig. 4**(c)** plots the force-displacement responses obtained from these two different honeycombs during the first cold programming cycle. Fig. 5 compares the mechanical metrics between these two honeycombs derived from the force-displacement curves in the first cycle.

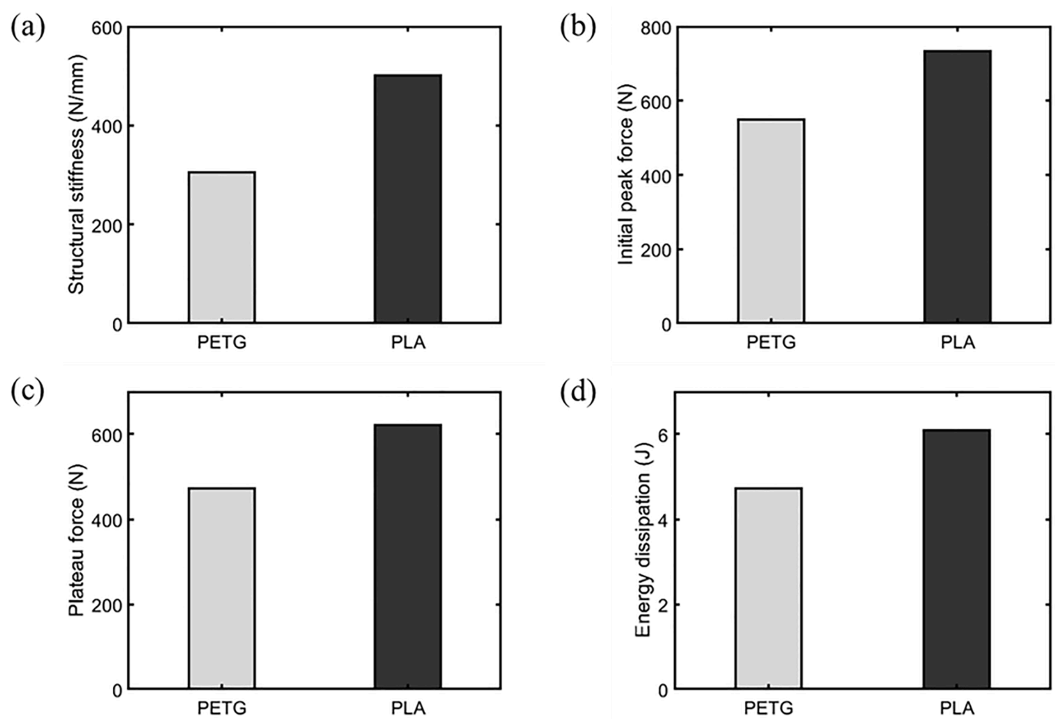

Fig. 5. Comparison of the mechanical metrics of hexagonal honeycombs printed with different constituent materials in the first cold programming cycle: (a) structural stiffness, (b) initial peak force, (c) plateau force, (d) energy dissipation. The PLA hexagonal honeycomb outperforms the PETG counterpart, indicating constituent materials have an effect on the mechanical performance of metamaterials.

Apparently, the PLA hexagonal honeycomb exhibits certain advantages in terms of all the metrics over the PETG counterpart. Fig. 5**(a)** shows that the PLA hexagonal honeycomb had a structural stiffness of 502 N/mm in the first cycle, which was 39% higher than that of the PETG hexagonal honeycomb (302 N/mm). Fig. 5**(b)** indicates the initial peak force of the PLA hexagonal honeycomb in the first cycle was 734 N, 25% higher than that of the PETG counterpart (548 N). Fig. 5**(c)** shows the PLA hexagonal honeycomb exhibited a plateau force of 621 N in the first cycle, 24% higher than that of the PETG counterpart (472 N). Fig. 5**(d)** reveals that the energy dissipation capacity of the PLA hexagonal honeycomb during the first cycle was 6.09 *J*, which is 22% higher than that of the PETG hexagonal honeycomb (4.72 *J*).

The PLA metamaterial exhibited a higher structural stiffness might be due to its higher elastic modulus (c.f. Fig. 5**(b)**), which also achieved a higher initial peak force and higher plateau force. 3D-printed metamaterials are believed to inherit the mechanical properties of their constituent materials. The slender wall segments of honeycombs experienced a series of local bending/buckling during compression, which can be observed from both experimental results and numerical results (to be shown in Figs. 7 and 8). Since the critical buckling load is proportional to the elastic modulus of constituent material, the PLA honeycomb can withstand a higher load than the PETG honeycomb prior to local buckling, resulting in a greater initial peak force and greater plateau force. Note that the higher structural stiffness, greater initial peak force and plateau force of the PLA honeycomb contribute to a larger area enclosed by the loading-unloading curve. As a result, the PLA honeycomb dissipated more energy than the PETG counterpart during the first cold programming cycle.

3.1.3. Effect of unit-cell structures

In addition to the printing materials, the unit-cell structures also play a significant role in impacting the mechanical characteristics of honeycomb metamaterials. The effect of unit-cell structures was analyzed based on the PETG honeycomb samples with different unit-cell structures. Fig. 4**(b)** plots the force-displacement responses obtained from the first cold programming cycle for the hexagonal, the hybrid, and the re-entrant honeycombs.

Fig. 6 compares the derived mechanical metrics of these three PETG honeycombs in the first cycle. Fig. 6**(a)** shows that the re-entrant honeycomb exhibited the highest structural stiffness of 692 N/mm. In comparison, the hybrid and the hexagonal honeycombs were of structural stiffnesses of 493 N/mm and 305 N/mm, respectively, which were 29% and 56% lower than the re-entrant counterpart. Fig. 6**(b)** shows that the re-entrant honeycomb had an initial peak force of 766 N in the first cycle, which was 10% and 28% higher than those of the hybrid (686 N) and the hexagonal (548 N) counterparts, respectively. Fig. 6**(c)** indicates that the re-entrant honeycomb provided a plateau force of 595 N, which was 1% and 21% higher than those of the hybrid (591 N) and hexagonal (472 N) counterparts, respectively. Fig. 6**(d)** reveals that the re-entrant honeycomb dissipated 6.30 *J* energy during the first cycle. In contrast, the hybrid and hexagonal honeycombs dissipated 6.19 *J* (2% lower) and 4.72 *J* (25% lower) of energy, respectively.

The quantitative comparison reveals that the re-entrant honeycomb exhibited the best mechanical performance, followed by the hybrid and then the hexagonal counterparts. The main reason is that these three honeycombs have distinct deformation patterns due to different Poisson's ratios.

For the hexagonal honeycomb, the material expanded horizontally under vertical compression due to a positive Poisson's ratio. This led to the formation of a shear band along the diagonal direction of the honeycomb structure during compression, as shown in Fig. 7**(a)**. The presence of the shear band significantly reduced the stiffness and strength of the hexagonal honeycomb, as the majority of plastic deformation was concentrated in the shear band. As a result, the hexagonal honeycomb dissipated the least energy in the first cycle of compression among these three honeycomb configurations.

For the re-entrant honeycomb, however, its overall negative Poisson's ratio caused the structure to contract horizontally when being compressed vertically. Fig. 7**(c)** shows that the material continuously flew towards the central region of the re-entrant honeycomb during the

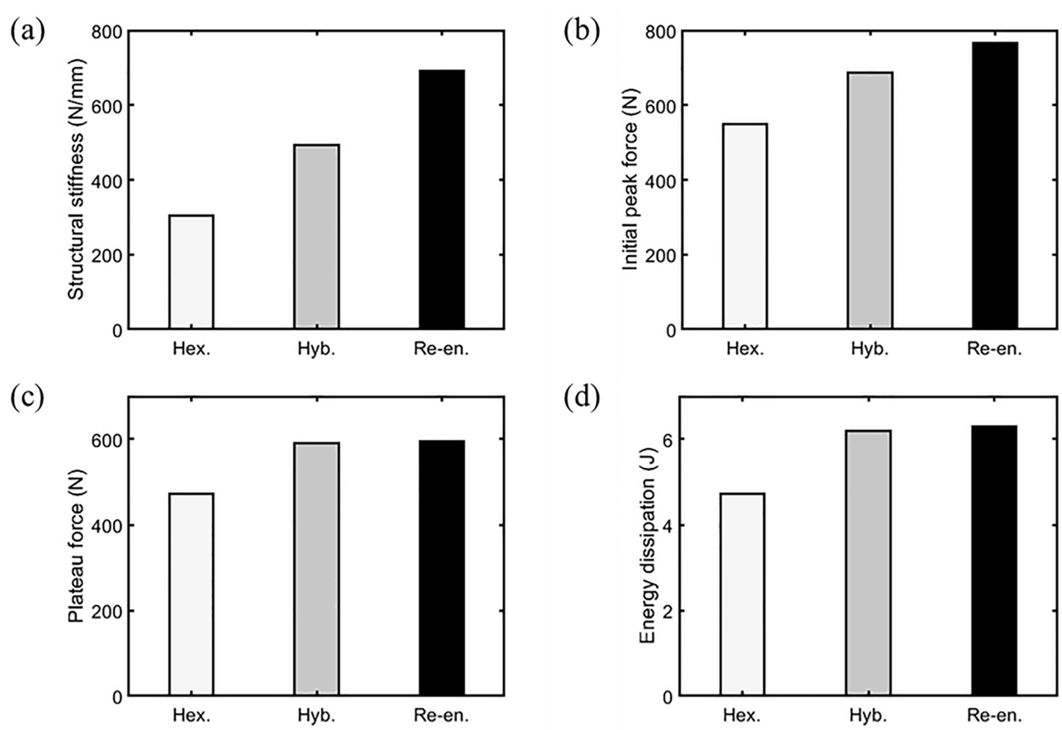

Fig. 6. Mechanical metrics for PETG metamaterials printed with different unit-cell configurations in the first cold programming compression cycle: (a) structural stiffness, (b) initial peak force, (c) plateau force, (d) energy dissipation. The re-entrant honeycomb outperforms the hybrid honeycomb, which in turn outperforms the hexagonal honeycomb, indicating unit-cell geometry has an effect on the mechanical performance of metamaterials.

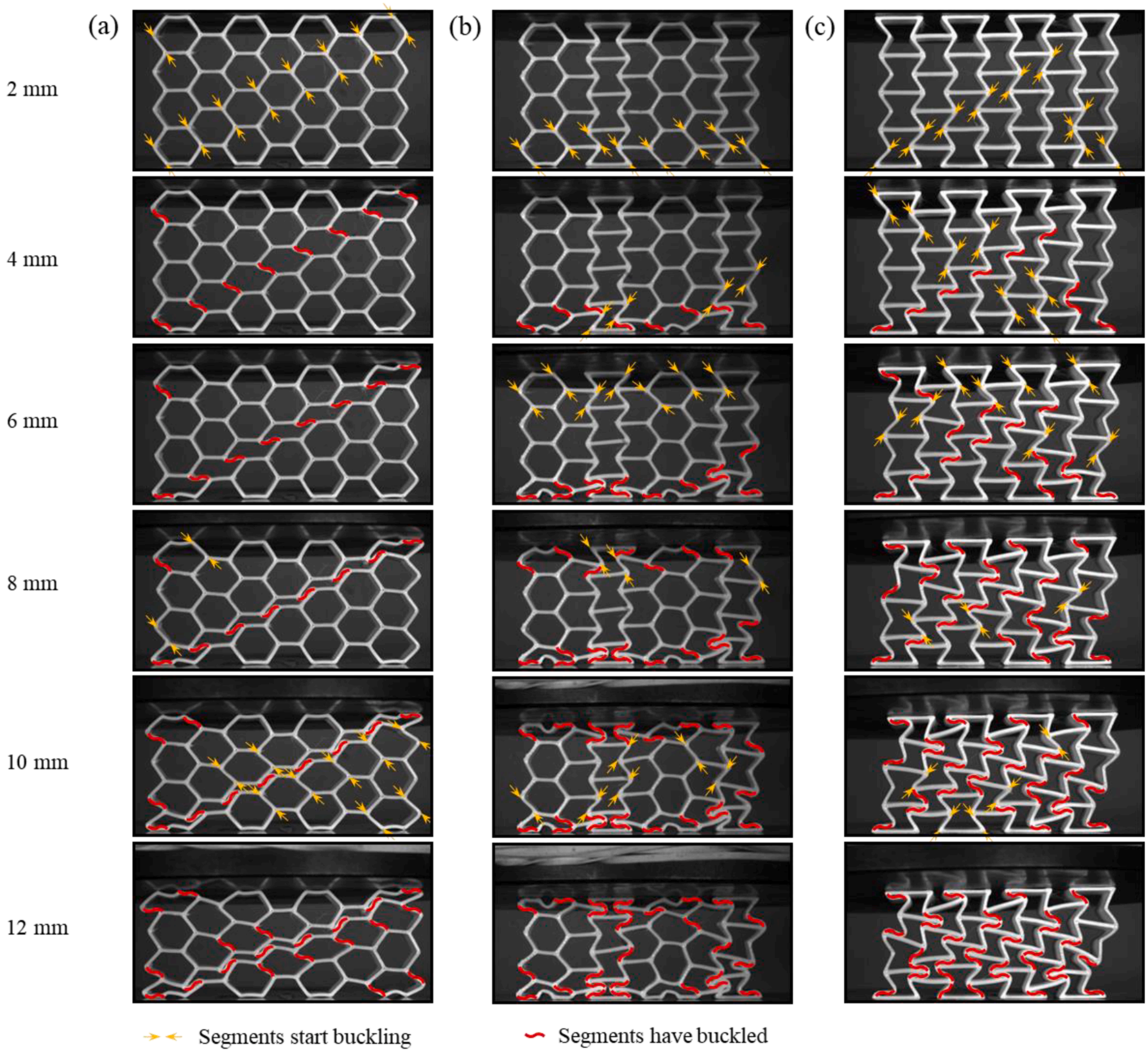

Fig. 7. Deformation patterns of the honeycombs with different unit-cell configurations during compression: (a) the hexagonal honeycomb with deformation concentrated on a shear band, (b) the hybrid honeycomb with deformation occurred in the top and bottom layers of unit-cells, (c) the re-entrant honeycomb with a more uniformly distributed deformation.

compression process. This auxetic characteristic allowed for the formation of a uniform deformation pattern in the re-entrant honeycomb. Since plastic deformation was uniformly distributed throughout the honeycomb instead of being concentrated on the shear band, more material in the re-entrant honeycomb experienced plastic deformation than in the hexagonal counterpart overall. This led the re-entrant honeycomb to exhibit higher structural stiffness and strength, thereby dissipating more energy than other honeycomb counterparts.

On the other hand, the hybrid honeycomb underwent no lateral contraction or expansion under compression due to a zero overall Poisson's ratio. This is because the hybrid honeycomb has an alternating arrangement of the hexagonal and re-entrant uni-cells in each layer. When being compressed, the hexagonal cells expand laterally whilst the re-entrant cells contract. Once the unit cell initiates deformation, it triggers its adjacent cells in the same layer (with different unit-cell structures) to deform significantly as well, as shown in Fig. 7**(b)**. This led to most plastic deformation being concentrated in the top and bottom layers of the hybrid honeycomb during the compression. Since the overall plastic deformation in the hybrid honeycomb lies in between the hexagonal honeycomb and the re-entrant honeycomb, it exhibited some intermediate mechanical performance overall.

The different Poisson's ratios exhibited by different honeycombs stem from the different orientations of struts within the honeycomb structure, which influence how the structure deforms under stress. As shown in Fig. 8**(a)**, the hexagonal honeycomb has convex cells with outward angles. Therefore, the hexagonal unit cell has its inclined segments bending outward after buckling until they come into contact with inclined segments from adjacent cells to achieve localized compactness. During this process, the inclined segments horizontally push neighboring cells away, resulting in a positive Poisson's ratio. In comparison, the re-entrant honeycomb has concave cells with inward angles. Accordingly, the inclined segments of the re-entrant unit cell bend inward after buckling and eventually contact the horizontal segments from the same cell to achieve localized compactness. Consequently, the neighboring cells are pulled closer horizontally, leading to a negative Poisson's ratio of the re-entrant structure.

Numerical simulations of the deformation process of honeycombs under quasi-static compression were conducted using the finite element analysis (FEA) method to validate the experimental analysis. The details of the FEA setup can be found in the Appendix. Fig. 8 indicates the agreement between experimental and numerical results. The deformation patterns of the hexagonal and re-entrant honeycombs at the maximum compression displacement during the experiment (in Fig. 8 **(a)**) closely match that from the simulation (in Fig. 8**(b)**).

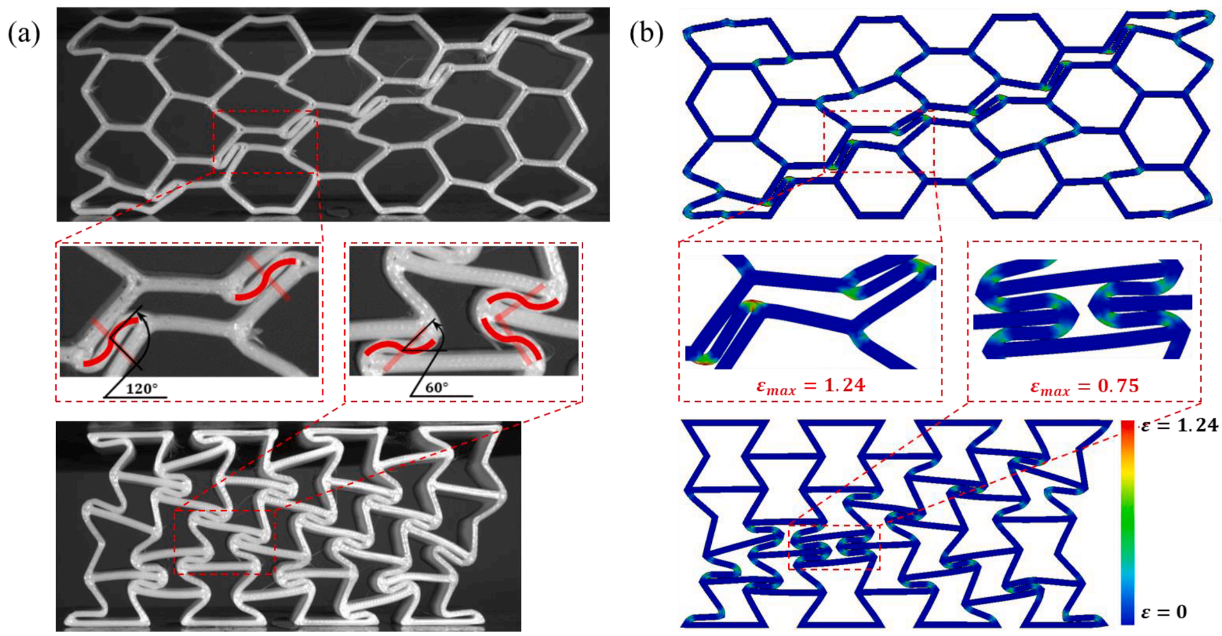

Fig. 8. Comparison of deformation patterns between the hexagonal honeycomb and the re-entrant honeycomb. (a) The experimental result. (b) The numerical result. The plastic strain concentrates in diagonal cells within the hexagonal honeycomb but spreads more uniformly within the re-entrant honeycomb. Numerical results show that the maximum plastic strain in the hexagonal honeycomb (1.24) is approximately 40% higher than that in the re-entrant honeycomb (0.75).

3.2. Reusability of metamaterials

The above analysis on the effects of printing materials and unit-cell structures on the mechanical performance of metamaterials was based on the experimental data obtained from the first cold programming cycle of compression. As all the honeycomb samples were fabricated with shape memory polymers, these samples have the potential for recurring energy dissipation as the residual plastic strain is recoverable after unloading in each cycle simply following a heating process. Thus, the honeycomb samples were performed with consecutive cold programming cycles for the reusability study.

In this section, the experimental data of each honeycomb sample was

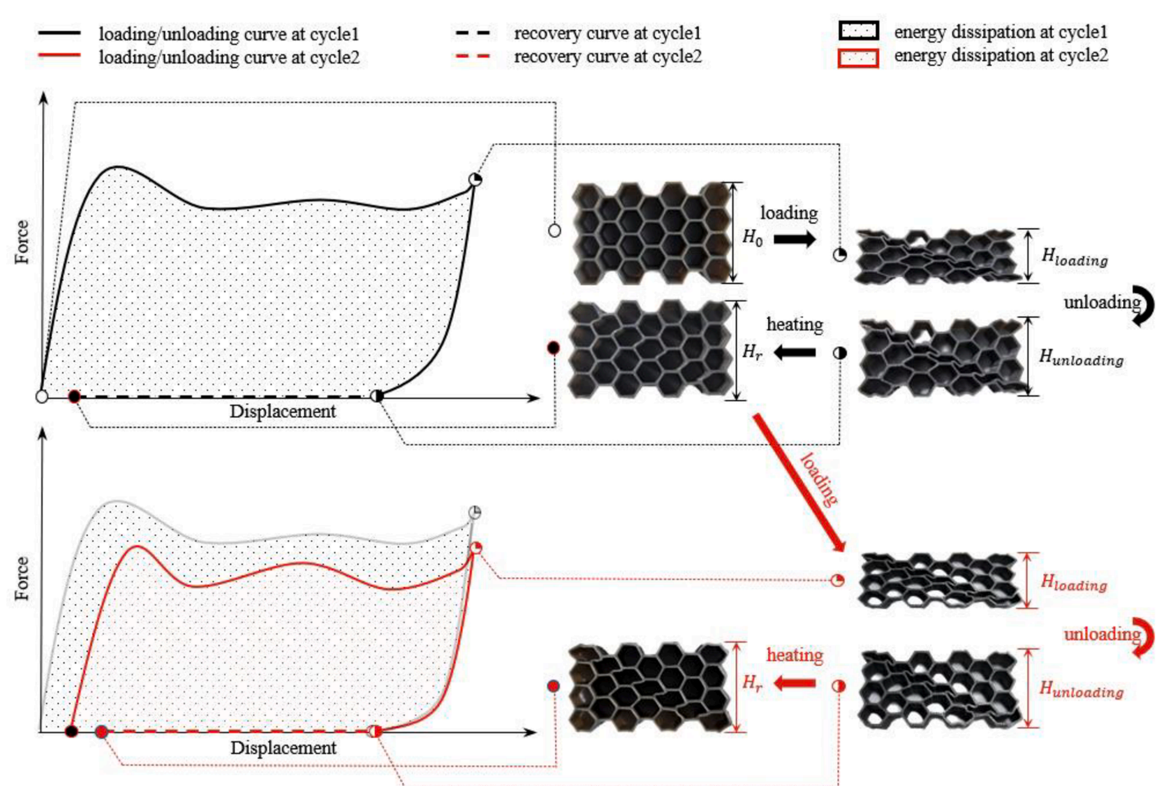

Fig. 9. A typical force-displacement response of honeycomb metamaterials from the cyclic cold programming process. The energy dissipating capability (the area between the loading and unloading curves) of metamaterials is expected to decrease, indicating the mechanical degradation of metamaterials during the process.

derived from multiple cold programming cycles with a constant compression distance of 12 mm (approximately 34% loading strain). The metrics used for the reusability analysis are introduced first, followed by the study on the influence of different heating media on the shape recovery of honeycombs to determine an optimal heating method. After that, the force-displacement responses of honeycomb samples derived from the cyclic cold programming tests and the reusability metrics obtained will be presented, followed by the analysis of the effect of printing materials and unit-cell structures on the reusability of the honeycomb metamaterials based on the reusability metrics.

3.2.1. Metrics for reusability analysis

The reusability analysis of metamaterials is based on the force-displacement curves obtained from the cyclic cold programming processes. Therefore, all the mechanical metrics introduced in Section 3.1.1 (e.g., energy dissipation (E_{diss})) at each cycle are used for the reusability analysis. It is worth noting that in some later cycles, the initial peak force may not be observed (which is believed to be caused by accumulated material damage and inadequate shape recovery). Thus, in these later cycles, the force at the transition from the elastic phase to the plastic phase was taken as F_{peak}.

Fig. 9 depicts the typical loading-unloading curves of the first two cold programming cycles. The degradation in mechanical metrics of honeycomb metamaterials occurs with increasing cycle numbers. For example, the energy dissipation capacity of the honeycomb in Cycle 2 (represented by the area embraced by the loading and unloading curves) is significantly lower than that in Cycle 1.

To characterize the reusability of honeycomb metamaterials, the remaining percentage of mechanical metrics (e.g., remaining energy dissipation percentage ($E_{diss\_rem}\%$)) was used to quantify the rate of mechanical degradation during cyclic testing. The remaining percentage for each mechanical metric is determined by dividing the current mechanical metrics obtained for honeycombs in a given cycle by the corresponding initial metrics measured in the first cycle. For example, $E_{diss\_rem}\%$ is calculated by $E_{diss\_rem}\% = \frac{E_{diss}}{E_{diss\_1st}} \times 100\%$, where E_{diss} represents the dissipated energy at the current cycle, and E_{diss_1st} denotes the initial energy dissipation at the first compression cycle. $E_{diss\_rem}\%$ can be used to reflect the ability of honeycombs to maintain the level of energy dissipation as the number of cycles increases. Likewise, the remaining percentage of other mechanical metrics can be calculated in a similar way.

In addition, the shape recovery ratio (R_r) is used to quantitatively describe the shape recovery of honeycomb metamaterials in cyclic testing. The height variation of the honeycomb during cyclic testing can be determined from the force-displacement curves in Fig. 9, where the honeycomb starts at an initial height, H_0, reaches $H_{loading}$ after compressive loading, rebounds to $H_{unloading}$ after unloading, and finally recovers to H_r after heating. In Cycle 1, H_0 is the initially designed height of the honeycomb sample. In the subsequent cycles, the H_0 becomes H_r from the previous cycle. Due to incomplete shape recovery, H_0 normally decreases in the subsequent cycles. This can typically be reflected in the rightward shift of the initial displacement value in the loading curve, indicating that the loading platen needs to move a longer distance to contact the upper surface of the sample from a fixed initial clearance. Note that the $H_{loading}$ remains the same for all the cycles because the cyclic compression employs a constant compression strain (34%), where the compression distance (D_{comp}) equals 12 mm. Since $H_{unloading}$ is the height recovered by the honeycomb through elastic deformation after unloading, its value generally decreases due to cumulative material damage during the cycle. This is reflected in the rightward shift of the final displacement value in the unloading curve, indicating that the loading platen moves a shorter distance from the maximum compression position, then no longer senses the reaction force from the honeycomb. In the final programming stage, the honeycomb undergoes stress-free shape recovery stimulated by heating, reaching the shape memory recovery height, H_r, which becomes a new initial height, H_0, for the next cycle.

Therefore, R_r at each cycle is calculated by $R_r = \frac{H_{ela}+H_{SME}}{D_{comp}} \times 100\%$, where $H_{ela} = H_{unloading} - H_{loading}$ is the height recovered from the elastic deformation during unloading, $H_{SME} = H_r - H_{unloading}$ is the height recovered through SME during heating. Thus, the numerator $H_{ela} + H_{SME} = H_r - H_{loading}$ represents the total height recovery that the honeycomb achieves at the end of each programming cycle. D_{comp} is the compression distance. R_r reflects the height recovery of honeycombs at the end of the cold programming process.

3.2.2. Heating method for SMP recovery

Shape memory polymers have a certain degree of hydrophilicity, meaning they can absorb moisture when placed in a humid environment, such as water. Most literature studies adopted water-bath heating as the triggering mechanism for the SME of SMPs [29,51,54,61,62]. However, there has been limited discussion on the influence of heating media on the shape recovery of SMPs. In this study, the honeycomb metamaterial samples were heated using water and air to investigate the influence of heating media.

Fig. 10**(a)** shows the water-heated cyclic cold programming results, in which the sample was submerged in a water bath (Joanlab, China) with a water temperature of 95 °C to heat for 30 s. Fig. 10**(b)** plots the air-heated cyclic cold programming results, in which the sample was placed into a preheated oven to conduct fan-forced heating at 95 °C for 3 min. The shape recovery ratios for each sample at the first four cycles were investigated. Fig. 10**(c)** exhibits that the water-bath heating method provided better shape recovery than the air-heating counterpart, with around 6% more recovery in each cycle (e.g., the shape recovery ratio of the air-heating method in Cycle 4 was 48.5%, whereas that of the water-bath heating method was 54.7%). Besides, the water-bath heating method was way more efficient than the air-heating method in triggering the SME of SMPs. The deformed honeycomb reversed most of its plastic deformation after about 180 s when heated with air (see Video 1 in the Supplementary material). In comparison, the same honeycomb achieved similar shape recovery within 8 s when heated with water (see Video 2 in the Supplementary material), which was 20 times more efficient than the air-heating method.

According to the principle of heat transfer in thermodynamics, the heat flux is proportional to the convective heat transfer coefficient (h) of media. The coefficient h of boiling water in free convection conditions is $2500-25{,}000\ W/(m^2 \cdot K)$, whereas the h of air in forced convection conditions is just $10-500\ W/(m^2 \cdot K)$. Therefore, water has a much greater heat transfer coefficient, allowing much faster heating on the samples. Considering shape recovery and experimental efficiency, the water-bath heating method was adopted as the means to trigger the shape memory effect of SMP honeycombs in this study.

3.2.3. Effect of printing materials

In this section, the experimental data of the PLA hexagonal honeycomb and the PETG hexagonal honeycomb from the first six cold programming cycles of compression is analyzed to investigate the effect of the printed constituent materials on the reusability of honeycomb metamaterials.

Figs. 11**(a)** and **(b)** display the force-displacement responses obtained from the first six cold programming cycles of the PLA and the PETG hexagonal honeycombs, respectively. Significant degradation is observed in the PLA hexagonal honeycomb because the increase in cycle numbers causes the force-displacement curve to shrink towards the bottom right, as indicated in Fig. 11**(a)**. In contrast, the PETG hexagonal honeycomb exhibits a marginal decrease in mechanical performance as the difference between the cyclic force-displacement curves is much less significant, as shown in Fig. 11**(b)**. An interesting finding is that an increasing force is observed at a displacement of around 9 mm in the force-displacement response of the PLA hexagonal honeycomb in later

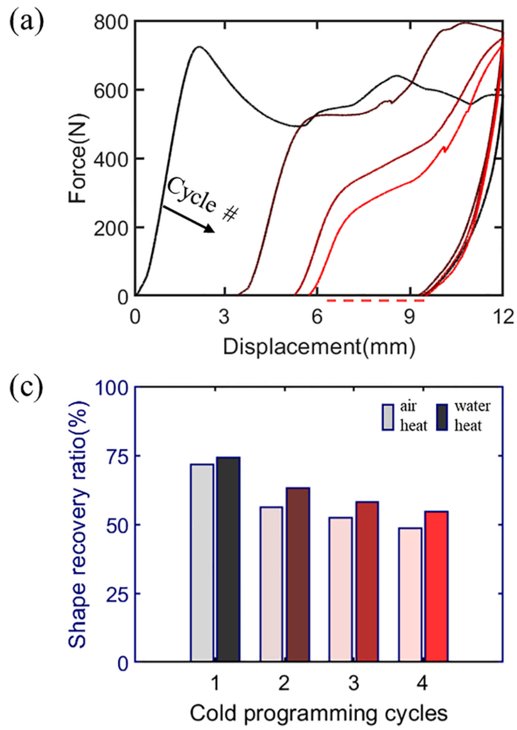

Fig. 10. Force-displacement responses of the PLA hexagonal honeycomb metamaterials from the different heating methods under the cyclic cold programming process. (a) The water-bath heating method. (b) The air-heating method. Colored solid lines in (a) and (b) refer to the force-displacement responses in the different cycles, while colored dashed lines depict the shape recovery due to the SME during the heating process at the last cycle. (c) Shape recovery ratios. The water-bath heating method provides better shape recoverability for the metamaterials than the air-based heating method.

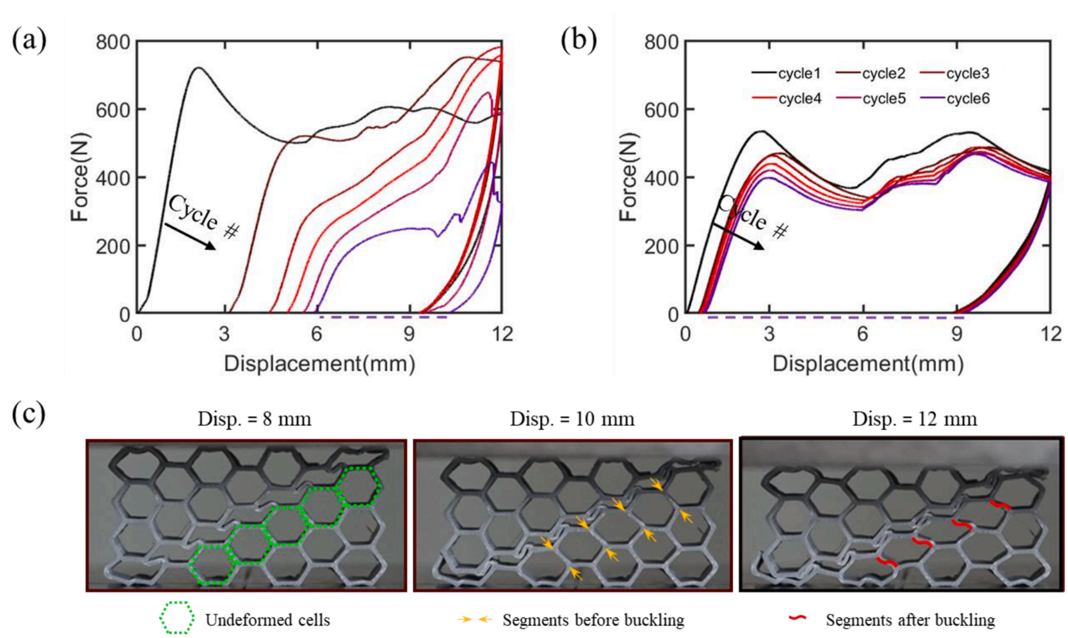

Fig. 11. Force-displacement responses of the hexagonal honeycomb metamaterials from the cyclic cold programming process. (a) The PLA hexagonal honeycomb. (b) The PETG hexagonal honeycomb. The PLA hexagonal honeycomb experiences more severe mechanical degradation than the PETG hexagonal honeycomb as the energy dissipation capacity (area between the loading-unloading curve) decreases more obviously. (c) Buckling occurred in the unit-cells on the secondary diagonal of the PLA hexagonal honeycomb in Cycle 2, causing the increase in force in the honeycomb.

cycles. This is believed to be related to the localized compactness that occurred on shear-band unit cells. As depicted in Fig. 11**(c)**, when the PLA honeycomb was compressed by 10 mm at Cycle 2, the inclined wall segments of cells along the secondary diagonal started undergoing more deformation to withstand the external load. This led to a continuous increase in force until the buckling took place at around 12 mm of displacement.

The reusability metrics for each honeycomb in each cycle were calculated and summarized in Fig. 12**(a)** to **(e)**. Fig. 12**(a)** shows that the structural stiffness of the PLA honeycomb experienced a significant

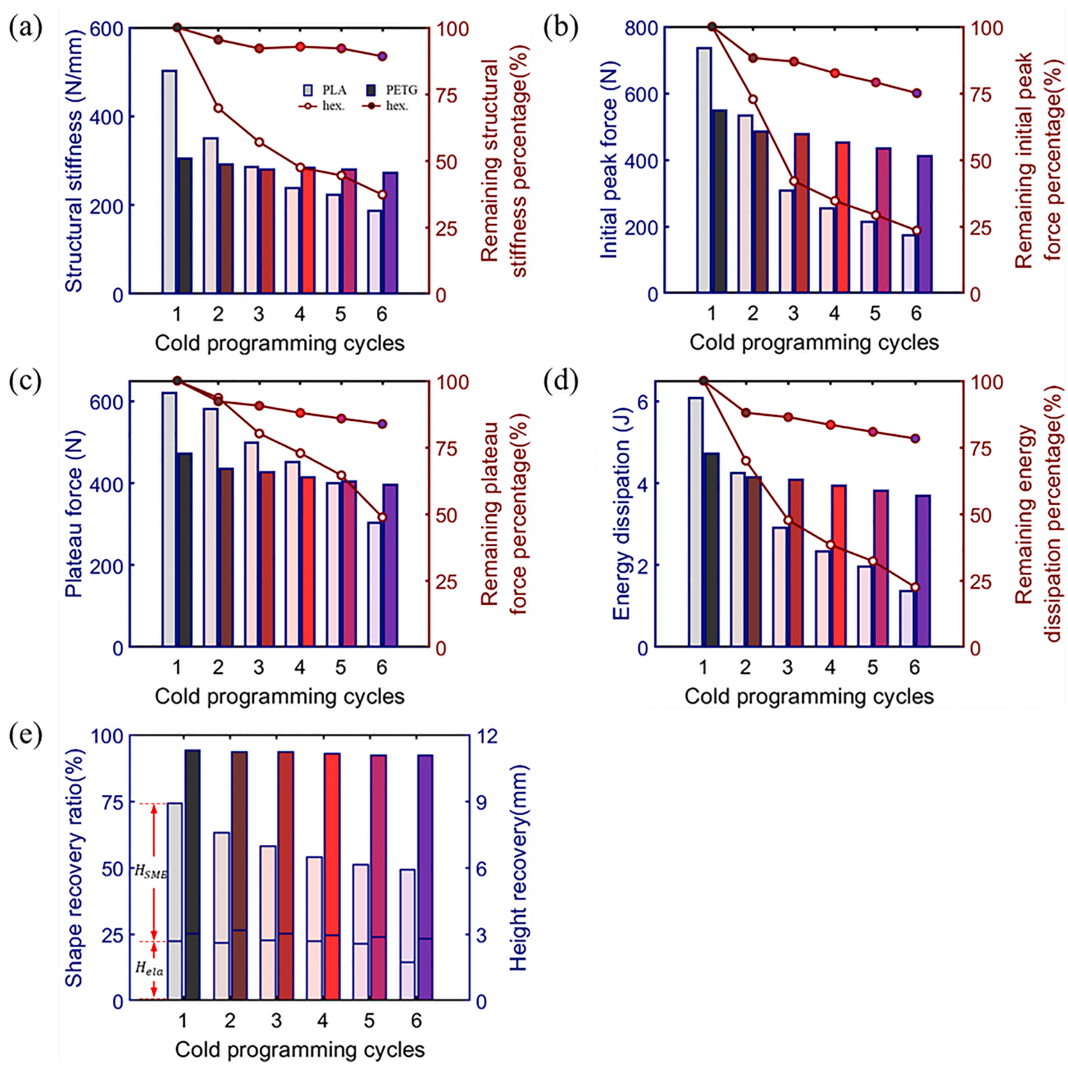

Fig. 12. Calculated reusability metrics for the hexagonal honeycomb metamaterials in each cold programming cycle based on corresponding cyclic force-displacement responses: (a) structural stiffness and its remaining percentage, (b) initial peak force and its remaining percentage, (c) plateau force and its remaining percentage, (d) energy dissipation and its remaining percentage, (e) shape recovery ratio and height recovery via elasticity and shape memory effect. The PLA hexagonal honeycomb exhibits more severe mechanical degradation than the PETG hexagonal honeycomb under cyclic cold programming.

reduction with increasing cycle numbers, starting from 502 N/mm in Cycle 1 and down to 187 N/mm (63% drop) in Cycle 6. In comparison, the structural stiffness of the PETG counterpart hexagonal honeycomb only decreased by 11% from 305 N/mm in Cycle 1 to 272 N/mm in Cycle 6. Although the PLA honeycomb had an initial structural stiffness 39% higher than the PETG counterpart, from Cycle 4 onwards, the structural stiffness of the PETG metamaterials started outperforming the PLA metamaterials.

A similar result can be observed in the initial peak force. Fig. 12**(b)** indicates that the initial peak force of the PLA hexagonal honeycomb reduced by 76.5% from 734 N to 172 N after six programming cycles, whereas the PETG counterpart only decreased by 25% from 548 N to 411 N. The slow degradation of PETG metamaterial hexagonal honeycomb enabled its initial peak force to surpass the PLA counterpart since Cycle 3.

Regarding the plateau force, the PETG hexagonal honeycomb also outperformed the PLA counterpart. Fig. 12**(c)** shows that the plateau force of the PLA metamaterial decreased from 621 N in Cycle 1 to 303 N in Cycle 6 (dropped by 51%). In comparison, the PETG metamaterial only decreased 16% in the plateau force from 472 N in Cycle 1 to 395 N in Cycle 6.

Due to the slower degradation of the stiffness, initial peak force, and plateau force during cold programming cycles, the PETG hexagonal honeycomb exhibited better capability in maintaining energy dissipation than the PLA counterpart. Fig. 12**(d)** shows that the PLA metamaterial provided an energy dissipation of 1.37 *J* in Cycle 6, which was only 22.5% of that in Cycle 1 (6.09 *J*). In contrast, while the PETG metamaterial dissipated 1.37 *J* less energy than the PLA counterpart in Cycle 1, it offered more energy dissipation from Cycle 3 onwards. The PETG honeycomb achieved an energy dissipation of 3.70 *J*, which was still 78.3% of that in Cycle 1.

All the above evidence indicates that the degradation of mechanical performance under cyclic working conditions is much more severe in the PLA hexagonal honeycomb than in the PETG counterpart. The main reason is that PLA has lower ductility than PETG, as demonstrated in Section 3.1.2. This makes the PLA honeycomb more prone to fracture than the PETG counterpart when undergoing the same level of plastic deformation.

Fig. 13**(a)** shows that cracks appeared in the shear-band unit-cells of the PLA hexagonal honeycomb only after two cycles. The cell at the bottom-left corner even had a complete nodal fracture. In addition, more and more cracks and complete nodal fractures occurred on the shear band as the programming cycle increased. In contrast, cracks accumulated much slower in the PETG counterpart. Only two minor cracks and

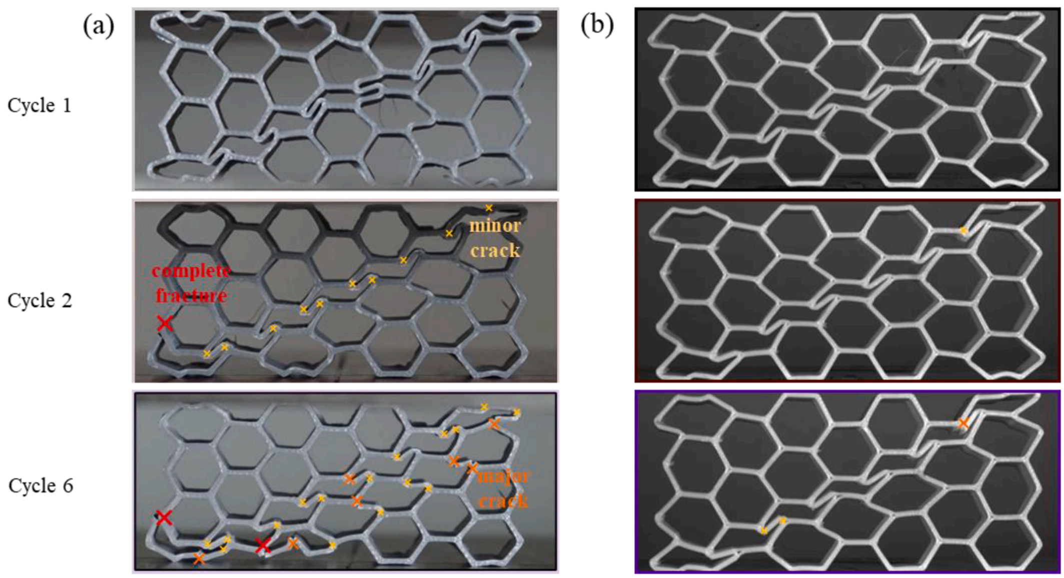

Fig. 13. Crack initiation and propagation of hexagonal honeycomb metamaterials at different cycles after unloading. (a) The PLA hexagonal honeycomb. (b) The PETG hexagonal honeycomb. The PLA hexagonal honeycomb is more prone to material failure than the PETG hexagonal honeycomb.

one major crack were observed in the PETG honeycomb in Cycle 6, and no cracks developed into complete nodal fractures (see Fig. 13**(b)**). The presence of nodal cracks and complete fractures significantly lowered the structural stiffness and strength of honeycombs. Thus, the PETG metamaterial exhibited much slower mechanical degradation than the PLA counterpart because the better ductility of PETG slowed down the initiation and propagation of cracks.

From the perspective of shape recovery ratio, the PETG hexagonal honeycomb showed better shape recovery capability than the PLA counterpart. Fig. 12**(e)** compares the shape recovery ratios and height recoveries between these two honeycombs during the cyclic tests. It can be observed that the PETG honeycomb achieved not only slightly higher recovered heights through elasticity but also significantly higher recovered heights through the SME compared to the PLA counterpart, exhibiting a superior overall shape recovery performance. For example, the shape recovery ratio of the PLA honeycomb in Cycle 1 was 74.1%, with a total height recovery of 8.89 mm (i.e., 2.66 mm from elastic deformation and 6.23 mm from the SME). In contrast, the PETG honeycomb achieved a much larger shape recovery ratio of 94.0%, with a total height recovery of 11.28 mm (i.e., 3.01 mm from elastic deformation and 8.27 mm from the SME). Furthermore, the PLA honeycomb experienced a more significant reduction in the shape recovery ratio than the PETG counterpart. The shape recovery ratio of the PLA metamaterial decreased from 74.1% in Cycle 1 to 49.3% in Cycle 6, a reduction of 24.8%, whereas the PETG hexagonal honeycomb had a shape recovery ratio of 92.3% in Cycle 6, only a 1.7% reduction compared to the 94.0% in Cycle 1.

Material damage in the node regions also played a dominant role in the overall shape recovery of honeycombs. As discussed in Section 2.2, the long molecular chains drive the shape memory effect of SMPs. Cracks and complete fractures at the nodes lead to the rupture of molecular chains, making it impossible to trigger the SME. As shown in Fig. 14**(a)**, the shear-banding cells with severe deformation in the PLA hexagonal honeycomb failed to recover to a hexagonal shape from Cycle 1 because of the failure of the constituent material. Moreover, the plastic deformation recovered by the SME in these cells became increasingly limited as the number of cycles increased. In contrast, Fig. 14**(b)** shows that the cells in the shear band of the PETG hexagonal honeycomb almost recovered to a perfect hexagonal shape even at the end of Cycle 6. Thus, the PETG hexagonal honeycomb always exhibited better shape

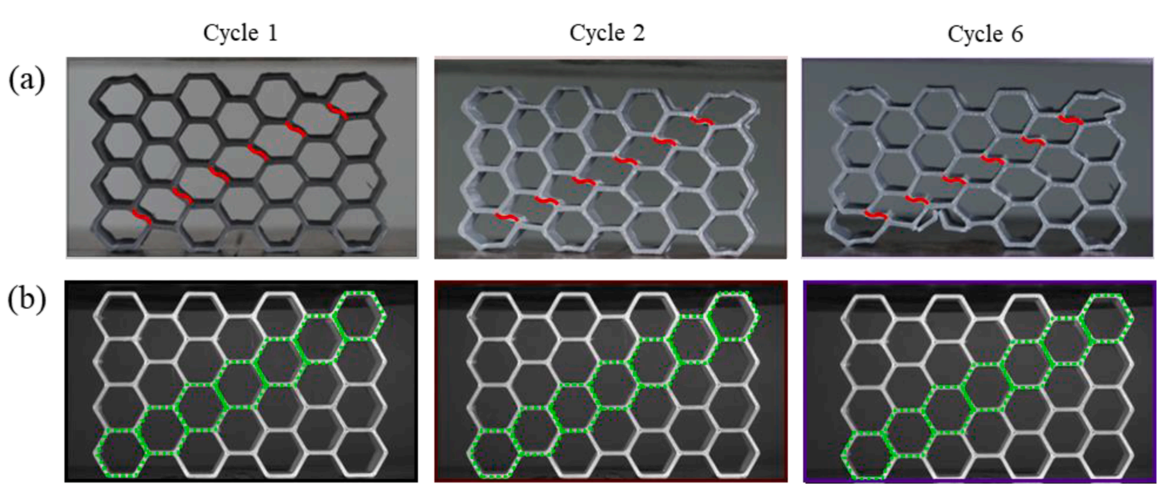

Fig. 14. Shape recovery of the hexagonal honeycomb metamaterials at different cycles after heating. (a) The PLA hexagonal honeycomb. (b) The PETG hexagonal honeycomb. The PLA hexagonal honeycomb fails to recover its initial shape from Cycle 1 due to severe material damage, while the PETG hexagonal honeycomb can still reverse to its initial shape in Cycle 6 due to less material damage.

recovery than the PLA counterpart in the same cycle due to the slower accumulation of material damage. The inadequate shape recovery reduces the mechanical performance of the PLA hexagonal honeycomb. This is because the wall segments stay in a buckling state even after heating, which reduces the overall structural stiffness and strength of the honeycomb.

Therefore, the PETG material shows excellent potential in cyclic working conditions due to its high fracture resistance. However, the significant mechanical degradation of the PLA material greatly hinders its reusable application in energy dissipation.

3.2.4. Effect of unit-cell structures

This section presents the results of PETG honeycombs with the hexagonal, the hybrid and the re-entrant configurations from cyclic cold programming tests. All the honeycomb samples were continuously programmed until their remaining energy dissipation capacity dropped to around 40% of the first cycle. The reusability metrics will be presented, followed by an analysis of the effect of unit-cell structures on the reusability of metamaterials.

Figs. 15**(a)** to **(c)** exhibit the results of the PETG hexagonal, the PETG hybrid and the PETG re-entrant honeycombs under multiple cycles, respectively. The hexagonal honeycomb was reused with 12 cycles before the remaining capacity of energy dissipation dropped to around 40%, which was three cycles and five cycles less than the hybrid honeycomb and the re-entrant honeycomb, respectively. Significant mechanical degradation was observed in the last few cycles for all honeycombs, manifested by a force decrease in the force-displacement responses. Fig. 15**(d)** demonstrates the abrupt drop in the force-displacement curve of the re-entrant honeycomb in Cycle 16 caused by a complete fracture at the node. The reusability metrics for each honeycomb at different cycles are summarized in Figs. 16**(a)** to **(e)**.

Fig. 16**(a)** shows that the structural stiffness of the hexagonal honeycomb gradually decreased from 305 N/mm in Cycle 1 to 74 N/mm in Cycle 12 (only 24% of Cycle 1). In comparison, the hybrid counterpart exhibited a decreasing structural stiffness from 493 N/mm in Cycle 1 to 293 N/mm in Cycle 12 (59% of Cycle 1), then further down to 149 N/mm in Cycle 15 (30% of Cycle 1). The structural stiffness of the PETG re-entrant honeycomb dropped from 692 N/mm in Cycle 1 to 532 N/mm in Cycle 12 (77% of Cycle 1), then to 278 N/mm in Cycle 15 (40% of Cycle 1), and finally to 159 N/mm in Cycle 17 (23% of Cycle 1). The re-entrant honeycomb exhibited the highest structural stiffness in each cycle, while the hexagonal honeycomb showed the lowest stiffness, with the hybrid honeycomb in between.

In terms of maintaining structural stiffness for recurring use, the re-entrant honeycomb outperformed the hybrid honeycomb and the hexagonal honeycomb. More specifically, based on a reference of approximately 30% of the remaining structural stiffness, the re-entrant metamaterial was reusable for 16 cycles (reduced to 35%), the hybrid metamaterial for 15 cycles (reduced to 30%), and the hexagonal metamaterial for only 12 cycles (reducing to 24%), which was four cycles less than that of the re-entrant counterpart.

Similar results can be observed in other reusability metrics. As shown in Fig. 16**(b)**, the re-entrant honeycomb consistently exhibited the highest initial peak force at any given cycle, while the hexagonal honeycomb displayed the least force, with the hybrid honeycomb in the middle. Moreover, taking approximately 30% of the remaining initial peak force percentage as a reference, the re-entrant honeycomb was reused for 15 cycles (reducing to 32%), which was one cycle more than the hybrid honeycomb (reducing to 33%) and four cycles more than the hexagonal honeycomb (reducing to 37%). Fig. 16**(c)** demonstrates that the re-entrant honeycomb consistently presented a higher plateau force at every cycle than the hybrid honeycomb, which, in turn, performed

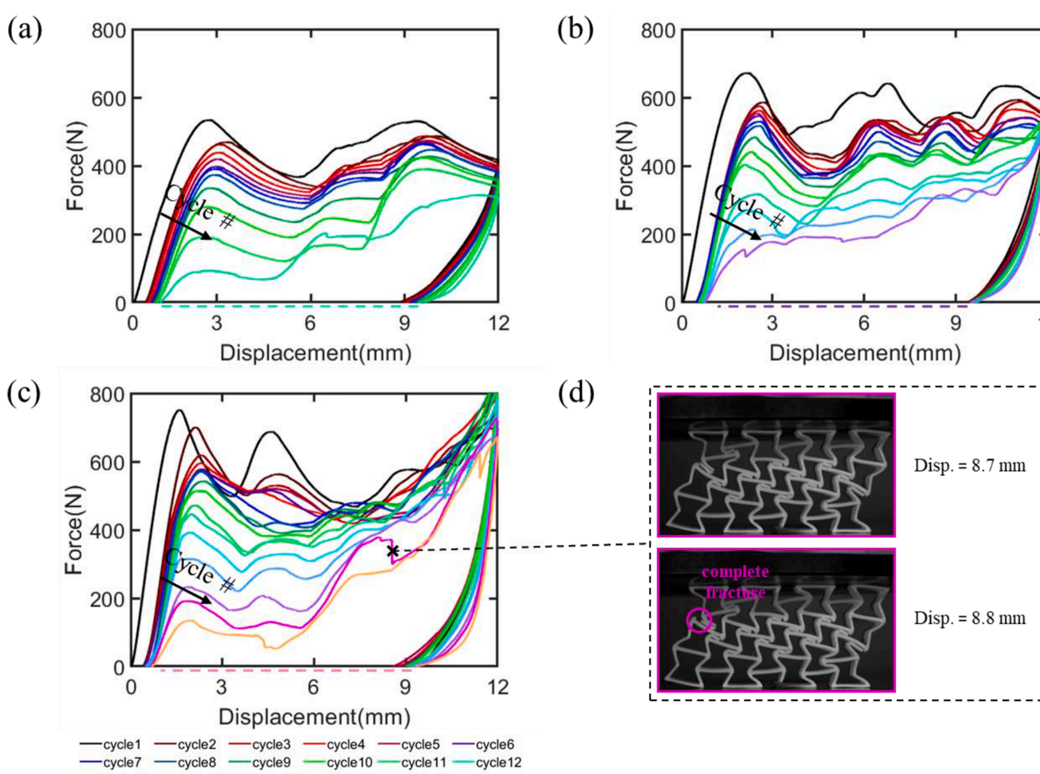

Fig. 15. Force-displacement responses of the PETG honeycomb metamaterials from the cyclic cold programming process. (a) The PETG hexagonal honeycomb. (b) The PETG hybrid honeycomb. (c) The PETG re-entrant honeycomb. Mechanical degradation is the most severe in the hexagonal honeycomb, followed by the hybrid honeycomb, and then the re-entrant honeycomb because it takes the hexagonal, the hybrid, and the re-entrant honeycombs 12, 15, and 17 cycles of cold programming, respectively, to have their remaining energy dissipation percentage decrease to approximately 40%. (d) A complete nodal fracture at the marked area in the re-entrant honeycomb causing a sudden drop in the force-displacement curve in (c).

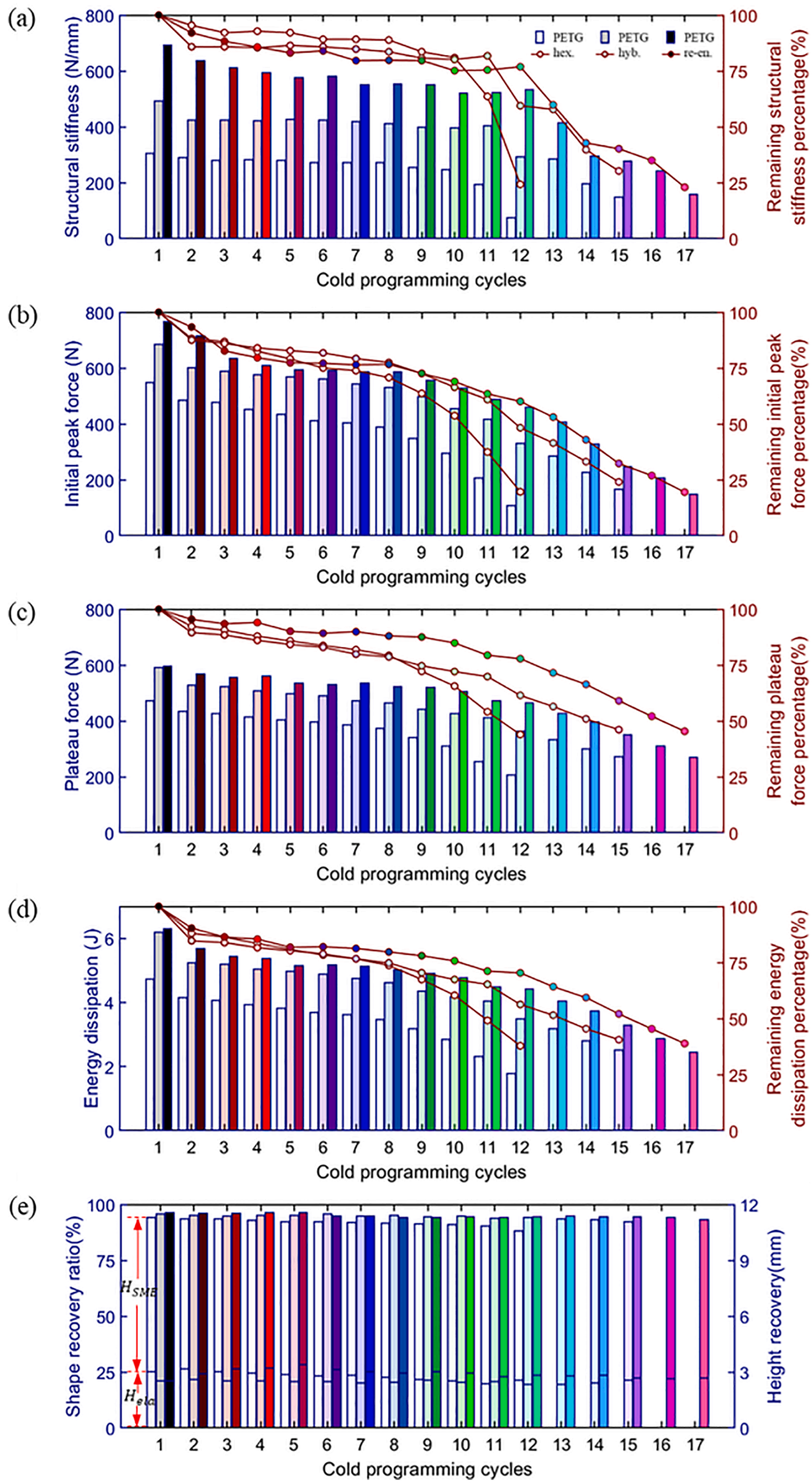

Fig. 16. Calculated reusability metrics for the PETG honeycomb metamaterials in each cold programming cycle based on corresponding cyclic force-displacement responses: (a) structural stiffness and its remaining percentage, (b) initial peak force and its remaining percentage, (c) plateau force and its remaining percentage, (d) energy dissipation and its remaining percentage, (e) shape recovery ratio and height recovery via elasticity and shape memory effect. Under cyclic cold programming, the mechanical degradation of the hexagonal honeycomb is the most severe, followed by the hybrid honeycomb, and then the re-entrant honeycomb.

better than the hexagonal honeycomb. Based on approximately 45% of the remaining plateau force percentage, the re-entrant honeycomb was reused for 17 cycles (reducing to 45%), which was two cycles more than the hybrid honeycomb (reducing to 46%) and five cycles more than the hexagonal honeycomb (reducing to 44%).

Fig. 16**(d)** indicates that, at each cycle, the re-entrant honeycomb consistently provided the highest energy dissipation, followed by the hybrid honeycomb and then the hexagonal honeycomb. Moreover, even after 17 reuse cycles, the re-entrant honeycomb still achieved a 39% remaining energy dissipation percentage. In comparison, the remaining percentage of the hybrid honeycomb was reduced to a similar level (40%) after 15 cycles, two cycles less than the re-entrant honeycomb. The hexagonal honeycomb was reused for 12 cycles, five cycles less than the re-entrant counterpart, before its remaining energy dissipation percentage decreased to 38%.

Fig. 16**(e)** shows that, in terms of shape recovery ratio, the re-entrant honeycomb performed the best, followed by the hybrid honeycomb, whereas the hexagonal honeycomb performed the worst. For example, the shape recovery ratio of the re-entrant honeycomb remained impressively at 94.6% in Cycle 12, with a total recovery height of 11.35 mm (2.85 mm from elastic deformation and 8.51 mm from the SME). In comparison, the shape recovery ratio of the hybrid honeycomb in that cycle was slightly lower at 94.0%, with a total recovery height of 11.28 mm (i.e., 2.35 mm from elastic deformation and 8.94 mm from the SME). The hexagonal honeycomb exhibited a shape recovery ratio of only 88.0%, with a total recovery height of 10.56 mm (i.e., 2.57 mm from elastic deformation and 8.00 mm from the SME), 0.79 mm less than the re-entrant counterpart. In addition, the shape recovery ratio of the re-entrant honeycomb decreased from 96.4% in Cycle 1 to 94.6% in Cycle 12, only a decrease of 1.8%. The hybrid honeycomb showed a similar reduction from 95.7% to 94.0%, a decrease of 1.7%. In contrast, the hexagonal honeycomb decreased from 94.0% to 88.0%, a decrease of 6.0%.

Another interesting finding is that with increasing cycles, the height recovered through elastic deformation in the re-entrant honeycomb remained similar, while that in the other two honeycombs gradually decreased. This suggests the advantage of the re-entrant structure in resisting material failure (i.e., with better remaining elastic recoverability) over the other two structures during cyclic cold programming.

The differences in reusability between honeycombs with different unit-cell structures are due to the strut angle between wall segments. As illustrated in Fig. 8**(a)**, the buckling segments of the re-entrant honeycomb require a rotation angle of 60° to achieve localized compactness. In contrast, the buckling segments of the hexagonal honeycomb require a rotation angle of 120°. This is because the re-entrant honeycomb achieves localized compactness after its inclined segments contact the horizontal segments within the same unit cell. In comparison, the inclined segments in the hexagonal honeycomb need to rotate until making contact with inclined segments from other cells to achieve localized compactness. Due to a larger rotation angle, the wall segments of the hexagonal honeycomb experience more severe deformation than that of the re-entrant honeycomb, potentially leading to more significant material damage.

The localized compactness prevents the deformed unit cell from further buckling, allowing the cell to transfer the applied force to other cells that have not undergone significant deformation, thereby facilitating subsequent buckling behavior. Due to the auxetic design, the re-entrant honeycomb can achieve local densification and make the transfer of force application more easily, which allows the cells of the re-entrant honeycomb to avoid excessive deformation and form a uniform distribution of plastic deformation at the maximum displacement (see Fig. 7). In comparison, the hexagonal metamaterial has plastic deformation concentrated on shear-banding cells, while the hybrid metamaterial presents the deformation in the cells at the top and bottom layers.

To quantitatively analyze the deformation, the plastic strains of the hexagonal and the re-entrant honeycombs at the maximum compression displacement were calculated using the FEA method. From Fig. 8**(b)**, the maximum plastic strain of the hexagonal honeycomb is computed as 1.24, while that of the re-entrant honeycomb is only 0.75 (about 40% lower). Moreover, the plastic strain of the hexagonal honeycomb is concentrated in the nodal regions of the diagonal cells. This means that material failure will initiate along the diagonal direction. In comparison, the plastic strain of the re-entrant honeycomb is distributed more uniformly, leading to less severe material failure over the honeycomb structure.

Less strain concentration made the re-entrant honeycomb more failure-resistant as the initiation and propagation of cracks were much slower. Fig. 17 illustrates the crack formation and propagation to complete nodal fractures in different honeycombs under cyclic cold programming. Fig. 17**(a)** shows that the hexagonal honeycomb experienced significant deformation in shear-banding cells. As a result, eight major cracks and three complete nodal fractures occurred by Cycle 12. In comparison, severe deformation occurred in the cells at both the top and bottom layers of the hybrid honeycomb. The cracks accumulated and propagated to fractures in the hybrid honeycomb much slower than in the hexagonal counterpart, with only five major cracks and one complete fracture occurring by Cycle 12, and twelve major cracks and three complete fractures by Cycle 15, as shown in Fig. 17**(b)**. Due to an overall uniform deformation, the crack accumulation and propagation was the slowest in the re-entrant honeycomb, with only two major cracks and one complete fracture occurring by Cycle 12, nine major cracks and two complete fractures by Cycle 15, and thirteen major cracks and five complete fractures by Cycle 17, see Fig. 17**(c)**. Thus, in terms of mechanical performance and resistance to mechanical degradation, the re-entrant honeycomb outperformed the hybrid honeycomb, whereas the hexagonal honeycomb was the worst.

4. Conclusions

In this study, shape memory polymer (SMP) honeycomb metamaterials were fabricated with PLA and PETG materials by using FDM technology. Cyclic cold programming tests were performed on prepared honeycomb samples to investigate the effect of printed materials and unit-cell structures on the mechanical characteristics and reusability of honeycomb metamaterials. Based on the experimental data obtained during cyclic tests, the following conclusions are drawn within its limitations:

The water-bath heating method not only provided 6% more shape recovery for honeycomb metamaterials than the air-based heating method but also showed 20 times more efficiency in triggering the shape memory effect of SMPs.

Under the one-off compression, the PLA hexagonal honeycomb exhibited better mechanical performance than the PETG counterpart because PLA has a more than double elastic modulus than PETG. Moreover, the PETG re-entrant honeycomb showed the best mechanical performance because it presented an overall uniform deformation pattern due to its negative Poisson's ratio. The PETG hybrid honeycomb exhibited an intermediate performance because it showed a deformation pattern with most plastic deformation residing in the top and bottom layers due to its zero Poisson's ratio. The PETG hexagonal honeycomb exhibited the worst performance because it presented a shear-band deformation due to its positive Poisson's ratio.

Under the cyclic cold programming, the PETG hexagonal honeycomb exhibited better reusability than its PLA counterpart, as the PETG honeycomb showed a remaining energy dissipation percentage of 78.3% at Cycle 6, nearly 3.5 times of the 22.5% of the PLA counterpart. This was because the better ductility of PETG not only slowed down mechanical degradation but also achieved better shape recovery to maintain structural stiffness and strength.

Under the cyclic cold programming, the PETG re-entrant honeycomb showed the best reusability in the three PETG honeycombs. The re-entrant honeycomb was reusable for 17 cycles to maintain about 40% of energy dissipation capacity, two cycles more than the hybrid counterpart and five cycles more than the hexagonal counterpart. This was because the re-entrant honeycomb experienced an overall uniform deformation pattern that caused the least strain concentration, thereby delaying crack formation and propagation. In contrast, the hybrid honeycomb had strain residing in the top and bottom layers of cells, thus showing an intermediate strain concentration. Due to the presence of the shear band, the hexagonal honeycomb experienced the most severe strain concentration that exacerbated the formation and propagation of

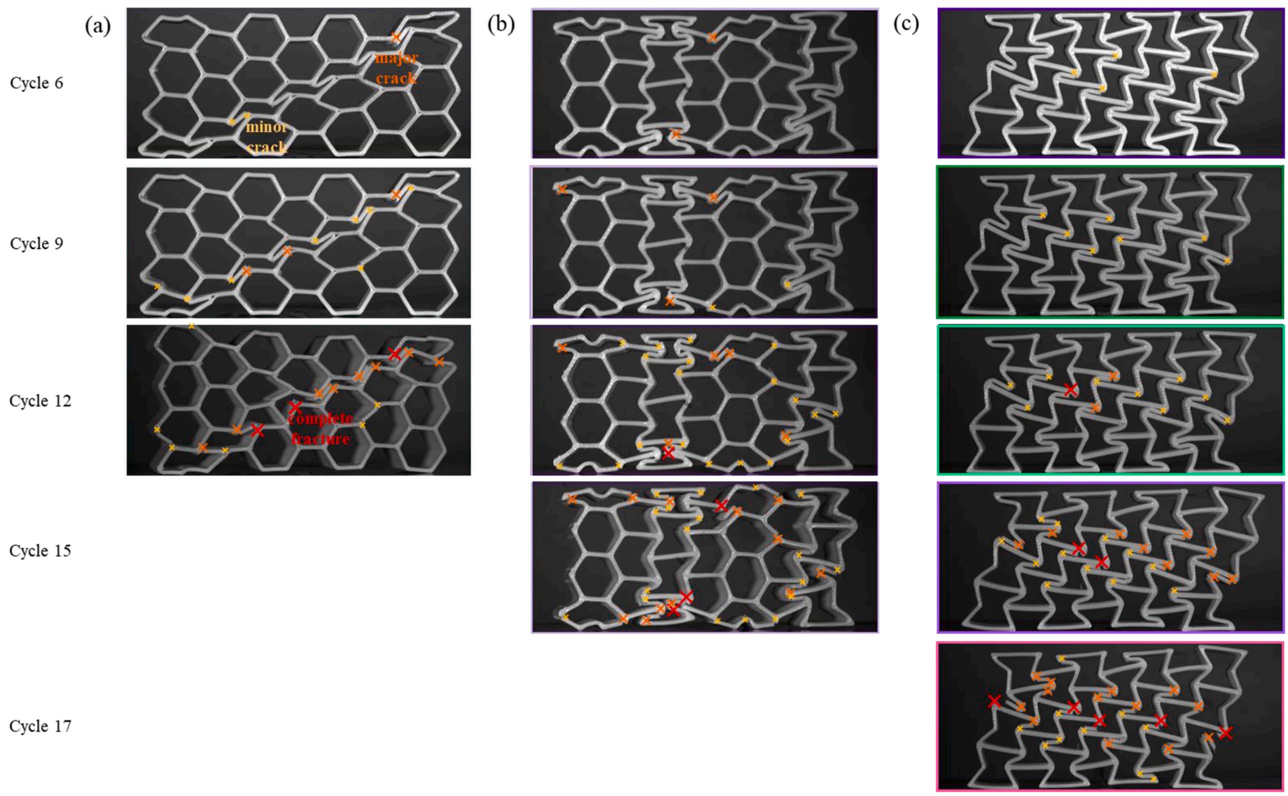

Fig. 17. Crack initiation, propagation, and development to complete nodal fractures at different cycles in different PETG honeycomb metamaterials. (a) The PETG hexagonal honeycomb. (b) The PETG hybrid honeycomb. (c) The PETG re-entrant honeycomb. The hexagonal honeycomb is the most prone to material failure, followed by the hybrid honeycomb and then the re-entrant honeycomb.

cracks.

Therefore, when applying metamaterials for reusable purposes, using constituent materials with better ductility and choosing failure-resistant structural designs (i.e., designs that introduce less strain concentration) are both considered effectivein achieving good reusability. In future work, other design strategies to enhance the reusability of metamaterials can be investigated, e.g., embedding honeycombs into foams to create composite materials [63], fabricating honeycombs with multimaterials [60,64–66], introducing disorder into honeycomb cells [67], adopting TPMS (Triply Periodic Minimal Surfaces) lattice structures [68]. Furthermore, it is necessary to employ advanced constitutive models [69,70] to simulate the shape memory effect of SMPs, and to explore the applications of reusable metamaterials in various fields such as aerospace [61] and soft robotics [71].

CRediT authorship contribution statement

Di Zhang: Data curation, Methodology, Software, Writing – original draft. **Meiyu Li:** Data curation, Investigation. **Na Qiu:** Data curation, Investigation, Methodology, Resources. **Jie Yang:** Data curation, Investigation. **Chi Wu:** Data curation, Investigation. **Grant Steven:** Funding acquisition, Supervision, Writing – review & editing. **Qing Li:** Funding acquisition, Supervision, Writing – review & editing. **Jianguang Fang:** Methodology, Project administration, Supervision, Writing – review & editing, Conceptualization, Funding acquisition.

Declaration of competing interest

The authors declare that they have no known competing financial interests or personal relationships that could have appeared to influence the work reported in this paper.

Data availability

Data will be made available on request.

Acknowledgments

The support from the Australian Research Council (ARC) Discovery scheme (DP190103752) is acknowledged. The first author is a recipient of the FEIT Scholarship and IRS Scholarship at the University of Technology Sydney. The last author is a recipient of the ARC Discovery Early Career Research Award (DE210101676).

Supplementary materials

Supplementary material associated with this article can be found, in the online version, at doi:10.1016/j.ijmecsci.2024.109309.

Appendix

The finite element analysis of honeycombs was performed using the explicit solver of LS-DYNA. The honeycombs were modeled using the solid element with an element size of 0.2 mm. The perfect plasticity material model was considered for simplification. The material properties of PETG (Polymaker, China), including a density of 1.25 g/cm^3, an elastic modulus of 0.70 GPa, a Poisson's ratio of 0.35, and a yield stress of 34.5 MPa, were adopted.

To numerically investigate the deformation process of honeycombs during the quasi-static compression in the vertical direction, the top rigid plate moved downward at a speed of 0.2 m/s, while the bottom rigid plate was fully constrained. The "automatic surface to surface" contact algorithm was used to model the contact between honeycombs and rigid plates, and the "automatic single surface" contact algorithm was used to model the self-contact of honeycombs. The static and dynamic coefficients of friction were both set to 0.25.

References

[1] Zadpoor AA. Mechanical meta-materials. Mater Horiz 2016;3(5):371–81. https://doi.org/10.1039/c6mh00065g.
[2] Surjadi JU, et al. Mechanical Metamaterials and Their Engineering Applications. Adv Eng Mater 2019;21(3). https://doi.org/10.1002/adem.201800864.
[3] Dogan E, Bhusal A, Cecen B, Miri AK. 3D Printing metamaterials towards tissue engineering. Appl Mater Today 2020;20. https://doi.org/10.1016/j.apmt.2020.100752. Sep.
[4] Fan J, et al. A review of additive manufacturing of metamaterials and developing trends. Mater Today 2021;50:303–28. https://doi.org/10.1016/j.mattod.2021.04.019.
[5] Jiao P, Alavi AH. Artificial intelligence-enabled smart mechanical metamaterials: advent and future trends. Int Mater Rev 2020;66(6):365–93. https://doi.org/10.1080/09506608.2020.1815394.
[6] de Jonge CP, Kolken HMA, Zadpoor AA. Non-auxetic mechanical metamaterials. Materials (Basel) 2019;12(4). https://doi.org/10.3390/ma12040635. Feb 20.
[7] Ren X, Das R, Tran P, Ngo TD, Xie YM. Auxetic metamaterials and structures: a review. Smart Mater Struct 2018;27(2). https://doi.org/10.1088/1361-665X/aaa61c.
[8] Kolken HMA, Zadpoor AA. Auxetic mechanical metamaterials. RSC Adv 2017;7(9): 5111–29. https://doi.org/10.1039/c6ra27333e.
[9] Balan P M, Mertens A J, Bahubalendruni MVAR. Auxetic mechanical metamaterials and their futuristic developments: a state-of-art review. Mater Today Commun 2023;34. https://doi.org/10.1016/j.mtcomm.2022.105285.
[10] Yu X, Zhou J, Liang H, Jiang Z, Wu L. Mechanical metamaterials associated with stiffness, rigidity and compressibility: a brief review. Prog Mater Sci 2018;94: 114–73. https://doi.org/10.1016/j.pmatsci.2017.12.003.
[11] Nicolaou ZG, Motter AE. Mechanical metamaterials with negative compressibility transitions. Nat Mater 2012;11(7):608–13. https://doi.org/10.1038/nmat3331. May 20,.
[12] Li H, Li Y, Li J. Negative stiffness devices for vibration isolation applications: a review. Adv Struct Eng 2020;23(8):1739–55. https://doi.org/10.1177/1369433219900311.
[13] Lakes RS, Lee T, Bersie A, Wang YC. Extreme damping in composite materials with negative-stiffness inclusions. Nature 2001;410(6828):565–7.
[14] Zheng X, et al. Ultralight, ultrastiff mechanical metamaterials. Science 2014;344 (6190):1373–7. https://doi.org/10.1126/science.1252291. Jun 20.
[15] Meza LR, Das S, Greer JR. Strong, lightweight, and recoverable three-dimensional ceramic nanolattices. Science 2014;345(6202):1322–6. https://doi.org/10.1126/science.1255908. Sep 12.
[16] Jang D, Meza LR, Greer F, Greer JR. Fabrication and deformation of three-dimensional hollow ceramic nanostructures. Nat Mater 2013;12(10):893–8. https://doi.org/10.1038/nmat3738. Oct.
[17] Askari M, et al. Additive manufacturing of metamaterials: a review. Add Manuf 2020;36. https://doi.org/10.1016/j.addma.2020.101562.
[18] Ryan KR, Down MP, Banks CE. Future of additive manufacturing: overview of 4D and 3D printed smart and advanced materials and their applications. Chem Eng J 2021;403. https://doi.org/10.1016/j.cej.2020.126162.
[19] Ngo TD, Kashani A, Imbalzano G, Nguyen KTQ, Hui D. Additive manufacturing (3D printing): a review of materials, methods, applications and challenges. Compos Part B Eng 2018;143:172–96. https://doi.org/10.1016/j.compositesb.2018.02.012.
[20] Zhang W, Xu J. Advanced lightweight materials for Automobiles: a review. Mater Des 2022;221. https://doi.org/10.1016/j.matdes.2022.110994.
[21] Yin H, Zheng X, Wen G, Zhang C, Wu Z. Design optimization of a novel bio-inspired 3D porous structure for crashworthiness. Compos Struct 2021;255. https://doi.org/10.1016/j.compstruct.2020.112897.
[22] Lee JY, An J, Chua CK. Fundamentals and applications of 3D printing for novel materials. Appl Mater Today 2017;7:120–33. https://doi.org/10.1016/j.apmt.2017.02.004.
[23] Zhang Z, Zhang L, Song B, Yao Y, Shi Y. Bamboo-inspired, simulation-guided design and 3D printing of light-weight and high-strength mechanical metamaterials. Appl Mater Today 2022;26. https://doi.org/10.1016/j.apmt.2021.101268.
[24] Zhilyaev I, Krushinsky D, Ranjbar M, Krushynska AO. Hybrid machine-learning and finite-element design for flexible metamaterial wings. Mater Des 2022;218. https://doi.org/10.1016/j.matdes.2022.110709.
[25] Wang Z, Li K, He Q, Cai S. A light-powered ultralight tensegrity robot with high deformability and load capacity. Adv Mater 2019;31(7):e1806849. https://doi.org/10.1002/adma.201806849. Feb.
[26] Wang C, Vangelatos Z, Grigoropoulos CP, Ma Z. Micro-engineered architected metamaterials for cell and tissue engineering. Mater Today Adv 2022;13. https://doi.org/10.1016/j.mtadv.2022.100206.
[27] Lin C, Liu L, Liu Y, Leng J. 4D Printing of Bioinspired Absorbable Left Atrial Appendage Occluders: a Proof-of-Concept Study. ACS Appl Mater Interfaces 2021; 13(11):12668–78. https://doi.org/10.1021/acsami.0c17192. Mar 24.
[28] Shi J, Zhu L, Li L, Li Z, Yang J, Wang X. A TPMS-based method for modeling porous scaffolds for bionic bone tissue engineering. Sci Rep 2018;8(1):7395. https://doi.org/10.1038/s41598-018-25750-9. May 9,.
[29] Namvar N, Zolfagharian A, Vakili-Tahami F, Bodaghi M. Reversible energy absorption of elasto-plastic auxetic, hexagonal, and AuxHex structures fabricated by FDM 4D printing. Smart Mater Struct 2022;31(5). https://doi.org/10.1088/1361-665X/ac6291.
[30] Lv W, Yu P, Li D. An energy dissipation metamaterial based on Coulomb friction and vibration. Int J Mech Sci 2024;263. https://doi.org/10.1016/j.ijmecsci.2023.108764.
[31] Deng F, Nguyen QK, Zhang P. Liquid metal lattice materials with simultaneously high strength and reusable energy absorption. Appl Mater Today 2022;29. https://doi.org/10.1016/j.apmt.2022.101671.
[32] Garland AP, et al. Coulombic friction in metamaterials to dissipate mechanical energy. Extreme Mech Lett 2020;40. https://doi.org/10.1016/j.eml.2020.100847.
[33] McCrary A, Hashemi MS, Sheidaei A. Programmable Bidirectional Mechanical Metamaterial with Tunable Stiffness and Frictional Energy Dissipation. Adv Theor Simul 2022;5(7). https://doi.org/10.1002/adts.202200135.
[34] Shi J, Mofatteh H, Mirabolghasemi A, Desharnais G, Akbarzadeh A. Programmable Multistable Perforated Shellular. Adv Mater 2021;33(42):e2102423. https://doi.org/10.1002/adma.202102423. Oct.
[35] Tan X, Chen S, Wang B, Zhu S, Wu L, Sun Y. Design, fabrication, and characterization of multistable mechanical metamaterials for trapping energy. Extreme Mech Lett 2019;28:8–21. https://doi.org/10.1016/j.eml.2019.02.002.
[36] Yang H, Ma L. Multi-stable mechanical metamaterials by elastic buckling instability. J Mater Sci 2018;54(4):3509–26. https://doi.org/10.1007/s10853-018-3065-y.
[37] Giri TR, Mailen R. Controlled snapping sequence and energy absorption in multistable mechanical metamaterial cylinders. Int J Mech Sci 2021;204. https://doi.org/10.1016/j.ijmecsci.2021.106541.
[38] Hua J, Zhou Y, Chen CQ. Design and analysis of a tunable multistable mechanical metamaterial. Int J Mech Sci 2024;272. https://doi.org/10.1016/j.ijmecsci.2024.109170.
[39] Wu L, Xi X, Li B, Zhou J. Multi-Stable Mechanical Structural Materials. Adv Eng Mater 2018;20(2). https://doi.org/10.1002/adem.201700599.
[40] Fu K, Zhao Z, Jin L. Programmable Granular Metamaterials for Reusable Energy Absorption. Adv Funct Mater 2019;29(32). https://doi.org/10.1002/adfm.201901258.
[41] Tibbits S. 4D Printing: multi-Material Shape Change. Archit Des 2014;84(1): 116–21. https://doi.org/10.1002/ad.1710.
[42] Yang H, D'Ambrosio N, Liu P, Pasini D, Ma L. Shape memory mechanical metamaterials. Mater Today 2023;66:36–49. https://doi.org/10.1016/j.mattod.2023.04.003.
[43] Qi J, et al. Recent Progress in Active Mechanical Metamaterials and Construction Principles. Adv Sci (Weinh) 2022;9(1):e2102662. https://doi.org/10.1002/advs.202102662. Jan.
[44] Montgomery SM, Kuang X, Armstrong CD, Qi HJ. Recent advances in additive manufacturing of active mechanical metamaterials. Curr Opin Solid State Mater Sci 2020;24(5). https://doi.org/10.1016/j.cossms.2020.100869.
[45] Demoly F, Dunn ML, Wood KL, Qi HJ, André JC. The status, barriers, challenges, and future in design for 4D printing. Mater Des 2021;212. https://doi.org/10.1016/j.matdes.2021.110193.
[46] Behl M, Lendlein A. Shape-memory polymers. Materials Today 2007;10(4):20–8. https://doi.org/10.1016/s1369-7021(07)70047-0.
[47] Hager MD, Bode S, Weber C, Schubert US. Shape memory polymers: past, present and future developments. Prog Polym Sci 2015;49-50:3–33. https://doi.org/10.1016/j.progpolymsci.2015.04.002.
[48] Xia X, Spadaccini CM, Greer JR. Responsive materials architected in space and time. Nat Rev Mater 2022;7(9):683–701. https://doi.org/10.1038/s41578-022-00450-z.
[49] Xu P, et al. Compression behavior of 4D printed metamaterials with various Poisson's ratios. Int J Mech Sci 2024;264. https://doi.org/10.1016/j.ijmecsci.2023.108819.
[50] Wan M, Yu K, Sun H. 4D printed programmable auxetic metamaterials with shape memory effects. Compos Struct 2022;279. https://doi.org/10.1016/j.compstruct.2021.114791.
[51] Zeng C, Liu L, Bian W, Leng J, Liu Y. Temperature-dependent mechanical response of 4D printed composite lattice structures reinforced by continuous fiber. Compos Struct 2022;280. https://doi.org/10.1016/j.compstruct.2021.114952.
[52] Dong K, Wang Y, Wang Z, Qiu W, Zheng P, Xiong Y. Reusability and energy absorption behavior of 4D printed continuous fiber-reinforced auxetic composite structures. Compos Part A Appl Sci Manuf 2023;169. https://doi.org/10.1016/j.compositesa.2023.107529.
[53] Wan M, Yu K, Gu J, Zeng H, Sun H, Khatibi AA. 4D printed TMP origami metamaterials with programmable mechanical properties. Int J Mech Sci 2023; 250. https://doi.org/10.1016/j.ijmecsci.2023.108275.
[54] Hamzehei R, Serjouei A, Wu N, Zolfagharian A, Bodaghi M. 4D Metamaterials with Zero Poisson's Ratio, Shape Recovery, and Energy Absorption Features. Adv Eng Mater 2022;24(9). https://doi.org/10.1002/adem.202200656.
[55] Wang K, Sun G, Wang J, Yao S, Baghani M, Peng Y. Reversible energy absorbing behaviors of shape-memory thin-walled structures. Eng Struct 2023;279. https://doi.org/10.1016/j.engstruct.2023.115626.
[56] Sun G, Wang J, Wang K, Baghani M, Peng Y, Rao Y. Repeatable compressive functionality of 3D printed shape-memory thin-walled corrugated structures. Int J Mech Sci 2023;257. https://doi.org/10.1016/j.ijmecsci.2023.108552.
[57] Zhang X, et al. Bio-inspired 4D printed intelligent lattice metamaterials with tunable mechanical property. Int J Mech Sci 2024;272. https://doi.org/10.1016/j.ijmecsci.2024.109198.

[58] Liu C, Qin H, Mather PT. Review of progress in shape-memory polymers. J Mater Chem 2007;17(16). https://doi.org/10.1039/b615954k.
[59] Gao G, Xu F, Xu J, Tang G, Liu Z. A Survey of the Influence of Process Parameters on Mechanical Properties of Fused Deposition Modeling Parts. Micromachines (Basel), 13; 2022. https://doi.org/10.3390/mi13040553. Mar 30.
[60] Bodaghi M, Serjouei A, Zolfagharian A, Fotouhi M, Rahman H, Durand D. Reversible energy absorbing meta-sandwiches by FDM 4D printing. Int J Mech Sci 2020;173. https://doi.org/10.1016/j.ijmecsci.2020.105451.
[61] Liu K, Wu J, Paulino GH, Qi HJ. Programmable Deployment of Tensegrity Structures by Stimulus-Responsive Polymers. Sci Rep 2017;7(1):3511. https://doi.org/10.1038/s41598-017-03412-6. Jun 14.
[62] Bodaghi M, Damanpack AR, Liao WH. Self-expanding/shrinking structures by 4D printing. Smart Mater Struct 2016;25(10). https://doi.org/10.1088/0964-1726/25/10/105034.
[63] Zolfagharian A, Picken P, Bodaghi M, Fard M, Rolfe B. Additive manufacturing of composite foam metamaterial springs for vibration isolation. Adv Eng Mater 2023;25(20). https://doi.org/10.1002/adem.202300356.
[64] Dong J, et al. Advanced design and fabrication of dual-material honeycombs for improved stiffness and resilience. Micromachines (Basel) 2023;14(11). https://doi.org/10.3390/mi14112120. Nov 18.
[65] Cheng Y, Li J, Qian X, Rudykh S. 3D printed recoverable honeycomb composites reinforced by continuous carbon fibers. Compos Struct 2021;268. https://doi.org/10.1016/j.compstruct.2021.113974.
[66] Ren L, et al. 4D printing of customizable and reconfigurable mechanical metamaterials. Int J Mech Sci 2024;270. https://doi.org/10.1016/j.ijmecsci.2024.109112.
[67] Bhuwal AS, Pang Y, Ashcroft I, Sun W, Liu T. Discovery of quasi-disordered truss metamaterials inspired by natural cellular materials. J Mech Phys Solids 2023;175. https://doi.org/10.1016/j.jmps.2023.105294.
[68] Novak N, et al. Quasi-static and dynamic compressive behaviour of sheet TPMS cellular structures. Compos Struct 2021;266. https://doi.org/10.1016/j.compstruct.2021.113801.
[69] Zolfagharian A, Jarrah HR, Xavier MS, Rolfe B, Bodaghi M. Multimaterial 4D printing with a tunable bending model. Smart Mater Struct 2023;32(6). https://doi.org/10.1088/1361-665X/accba8.
[70] Roudbarian N, Jebellat E, Famouri S, Baniasadi M, Hedayati R, Baghani M. Shape-memory polymer metamaterials based on triply periodic minimal surfaces. Euro J Mech ASolids 2022;96. https://doi.org/10.1016/j.euromechsol.2022.104676.
[71] Mohammadi M, et al. Sustainable robotic joints 4D printing with variable stiffness using reinforcement learning. Robot Comput Integr Manuf 2024;85. https://doi.org/10.1016/j.rcim.2023.102636.